Climate Dynamics (2025) 63:268
https://doi.org/10.1007/s00382-025-07760-2

Key local atmospheric processes of the heat extreme over the middle-lower Yangtze River basin in August 2022

Yue Sun[1] · Jianping Li[1,2] · Yang Zhao[1] · Hongyuan Zhao[1] · Hao Wang[1] · Mian Zhu[1] · Ning Wang[1]

Received: 24 March 2025 / Accepted: 9 June 2025

Abstract
The unprecedented heat event over the middle-lower Yangtze River Basin (YRB) in August 2022 had disastrous socio-economic impacts. Based on the general mechanism of multi-year surface air temperature (SAT) variation in August, this study focuses on the key local atmospheric processes responsible for the record-breaking event in 2022. We firstly propose that through hydrostatic adjustment, the local atmospheric perturbation thickness (APT) between 1000 and 500 hPa is the most crucial factor dynamically influencing the SAT over the YRB in August. Net diabatic heating from the surface affects the SAT thermodynamically at the same time. Analysis of the geopotential thickness tendency reveals that vertical motion (ω) and diabatic heating (Q) within the air column significantly affect the thickness of the air column in August, highlighting the pivotal role of the interaction among local APT,ω, and Q. The specific performance is that the downward motion and enhanced Q within the air column lead to increased local APT. Meanwhile, the increased APT and downward motion amplified the Q above the surface by reducing cloud cover. Therefore, thermodynamic processes are initiated by dynamic processes and exert a reciprocal influence on them. The results exhibit that this heat event was driven by both the hydrostatic adjustment of dynamic processes and diabatic heating of thermodynamic processes, with the dynamic processes playing a dominant role. Moreover, the APT and ω serve as crucial bridges through which upper-level atmospheric circulation affects the SAT. Additionally, despite these large-scale interannual processes, synoptic regional foehn effect should be taken into consideration.

Keywords Record-breaking heat event · Local atmospheric processes · Atmospheric perturbation thickness · Hydrostatic adjustment

1 Introduction

In August 2022, extreme and prolonged heatwaves struck the middle-lower Yangtze River basin (YRB). The maximum daytime (nighttime) maximum temperature in cities within the YRB reached 42 °C (30 °C), which set a new record (Yuan et al. 2023). From July 21 to August 30, the Central Meteorological Administration of China issued high-temperature warnings for 41 consecutive days, which were lifted on August 30. This climate event marked the most severe and large-scale heat and drought episode in this region since 1961. The extreme heat and drought triggered a series of adverse effects, including the Poyang Lake entering a drought period 100 days earlier than usual, with over 4.421 million square kilometers of arable land suffering reduced crop yields. Additionally, 4.99 million people and 920,000 livestock faced drinking water shortages (Xia et al. 2022), while Sichuan Province experienced power shortages and large-scale wildfires erupted in Chongqing (Lu et al. 2023).

Researchers have conducted extensive studies on this extreme event. The findings of Gong et al. (2024) indicated that all of the natural variability, anthropogenic forcing, and natural forcing have significant impacts on this event, with natural variability as the predominant factor accounting for 60% of the intensity of this extreme heat, which is primarily

✉ Jianping Li
ljp@ouc.edu.cn

[1] Frontiers Science Center for Deep Ocean Multi-Spheres and Earth System (DOMES)/Key Laboratory of Physical Oceanography/Academy of Future Ocean/College of Oceanic and Atmospheric Sciences/Center for Ocean Carbon Neutrality, Ocean University of China, Qingdao 266100, China

[2] Laboratory for Ocean Dynamics and Climate, Qingdao Marine Science and Technology Center, Qingdao 266237, China

Published online: 23 June 2025

attributed to the internal atmospheric circulations. About 50% of the intensity is linked to anthropogenic forcing, while the natural forcing (particularly the volcanic eruption in Tonga in early 2022) partially mitigated the warming effect of anthropogenic forcing, contributing around –10%. Additionally, the reduction of anthropogenic aerosols positively influenced the radiative balance, further contributing to this extreme heat event (Zhang et al. 2023a). In general, the atmospheric circulations associated with this extreme heat were not directly induced by external forcing, but were primarily driven by the atmospheric natural variability (Hua et al. 2023). Therefore, this study aims to figure out the key atmospheric processes that influenced this extreme heat event.

Among the atmospheric natural variabilities, local atmospheric factors are directly responsible for the occurrence of heat extremes. Existing studies have identified that strong downward motion at 500 hPa is the key local atmospheric factor featuring this extreme heat event (He et al. 2023; Hua et al. 2023; Tang et al. 2023; Wang et al. 2023; Yin et al. 2023; Yuan et al. 2024; Huang et al. 2024). The subsidence, primarily induced by the eastward extension of the south Asian high at 200 hPa and the westward extension of the northwestern Pacific subtropical high (NWPSH) at 500 hPa, reduced cloud cover and increased the shortwave radiation reaching the surface, elevating the surface air temperature (SAT). The overlap of mid- to upper-level (anticyclonic) high-pressure systems generated intense subsidence (Hua et al. 2023; Tang et al. 2023; Zhang et al. 2023b; Gong et al. 2024; Huang et al. 2024; Liao et al. 2024; Yuan et al. 2024). Additionally, the upper-level easterly wind anomaly is an important factor (He et al. 2023; Wang et al. 2023). The Tibetan Plateau acts as a heat source in summer, with the isentropic surfaces above it being lower than those in surrounding areas, and the YRB located at the south edge of the anomalous south Asian high and experienced anomalous easterly. Due to isentropic motion, the dry air advection caused by the local upper-level easterly wind also contributes to the initiation and maintenance of downward motion over the YRB. Therefore, the downward motion anomaly at 500 hPa, the mid- to upper-level geopotential height anomalies, and the upper-level zonal wind anomaly are closely linked with the anomalous SAT over the YRB.

Despite the above local dynamic processes, local thermodynamic processes may also play important roles. The positive feedback between soil moisture and air temperature played a significant role in amplifying the intensity of this extreme heat event. Specifically, the heatwave and drought in July 2022 significantly impacted the subsequent extreme heat in August through the soil moisture-temperature feedback mechanism (Jiang et al. 2023). Firstly, dry soil contributed to a decrease in near-surface water vapor, with more solar radiation reaching the land surface to warm the surface air. Secondly, reduced evaporation diminished the evaporative cooling effect and intensifying land-surface heating of the lower atmosphere, which dried the soil. Lastly, the increased surface temperature facilitated the maintenance of local high-pressure systems, inhibiting precipitation and further desiccating the soil, thereby forming a positive feedback (Fischer et al. 2007; Zhang and Wu 2011; Miralles et al. 2019; Wang et al. 2019; Thompson et al. 2022; Qiao et al. 2023; Gong et al. 2024; Ni et al. 2024). It is worth noting that there exists a nonlinear interaction between the land–atmosphere coupling within the natural variability and global warming induced by human forcing, with each factor serving to amplify the consequences of the other (Qiao et al. 2023; Zhou 2024).

Some researchers attempted to link SAT with local atmospheric perturbation thickness (APT). Struthwolf (1995) established empirical relationships between maximum SAT and APT under various weather conditions across different seasons, with all correlation coefficients exceeding 0.95. Massie and Rose (1997) found that the APT from the model forecasts could be used for SAT forecasting. Rose (2000) demonstrated that the APT could be successfully applied in operational forecasting for SAT. Darand (2020) showed that the correlation coefficients between the monthly averaged SAT and APT in 1000–500 hPa reached about 0.8 for all months. The theoretical basis for the linear relationship between APT and SAT lies in the quasi-hydrostatic balance within the atmosphere and the hydrostatic adjustment processes involved.

Quasi-hydrostatic balance and quasi-geostrophic balance are two essential equilibrium relations in the geophysical fluid dynamics. When a certain dynamic equilibrium is disrupted, physical mechanisms must act swiftly to restore it, allowing us to frequently observe these quasi-equilibrium states. These processes are defined as the adaptation of dynamic equilibrium (Ye and Li 1965). The perturbation hypsometric equation illustrates that the APT and the mean temperature anomaly mutually adapt to each other. Changes in the APT lead to corresponding changes in the mean temperature, and vice versa (Li et al. 2022). Through acoustic and acoustic gravity waves, the unbalanced energy between the thickness field and the temperature field in a confined space is dispersed throughout the entire space, resulting in the unbalanced energy in per unit volume approaching zero. Therefore, the fluctuations and imbalance phenomenon disappears, the field adaptation is completed, and a new equilibrium is formed (Hu and Zou 1991; Bannon 1995, 1996; Sotack and Bannon 1999; Chagnon and Bannon 2001; Cui et al. 2015, 2016). Acoustic and acoustic gravity waves propagate very fast in the atmosphere, so the hydrostatic adaptation process of the atmosphere is completed quickly. Therefore, APT may be one of the key factors influencing SAT over the YRB.

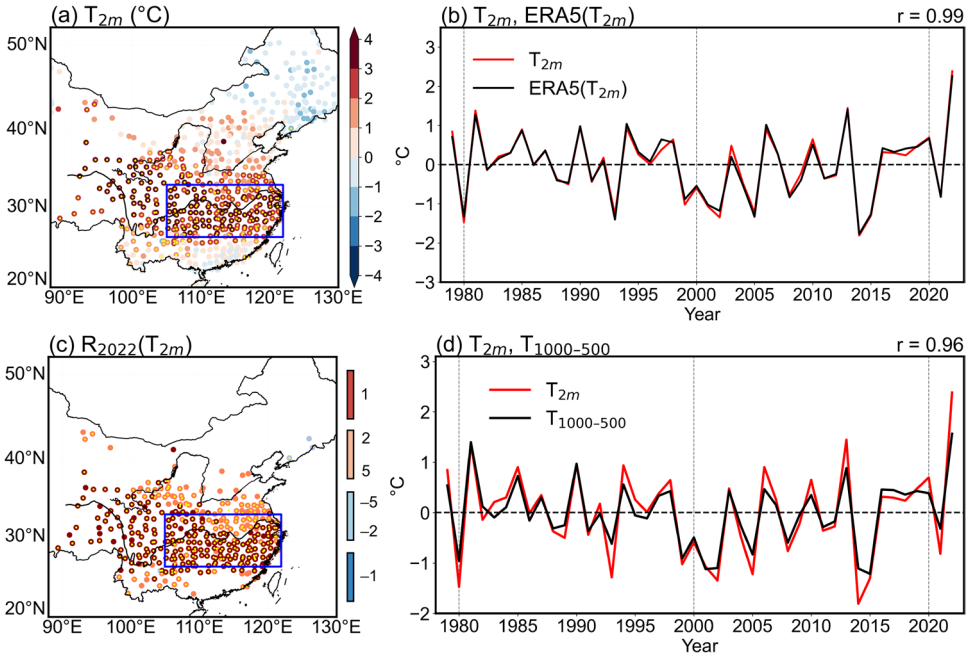

Fig. 1 **a** Anomalous monthly mean air temperature at 2-m height (T_{2m}) of gauge observation in August 2022 (red and blue dots, ℃), with a blue box (26°–33°N, 115°–122°E) indicating the domain of middle-lower Yangtze River basin (YRB) in this study (the same hereinafter). **b** Time series of areal mean T_{2m} anomalies of gauge observation (red line, ℃) and ERA5 (black line, ℃) in the YRB during 1979–2022. **c** Ranks of August T_{2m} (red and blue dots, ℃) in 2022 since 1979, with the positive values representing the rank from the maximum and the negative values from the minimum (the same hereinafter). **d** Time series of areal mean anomalies of T_{2m} from gauge observation (red line, ℃) and mean air temperature between 1000 and 500 hPa from ERA5 (black line, ℃) in the YRB during 1979–2022. Yellow dots in **a** and **c** indicate statistical significance of T_{2m} at the 95% confidence level. All the data in this work has been detrended (the same hereinafter)

Existing studies have provided a detailed analysis of this extreme heat event. However, there are still several issues that remain unresolved. First, the interactions and relative contributions among the key local atmospheric factors are unclear over the YRB in August. Second, the pathways by which upper-level atmospheric circulations influence the SAT are inconsistent, with ambiguous relationships among the upper-level factors. Therefore, this paper attempts to address the following two questions: What are the relationships and relative contributions among key local atmospheric processes responsible for this extreme heat event? Which mechanism links the upper-level atmospheric circulations to the SAT?

To solve above mentioned problems, this paper analyzes the role of APT as a local atmospheric factor in affecting SAT, explores the mechanisms underlying the variation of APT, and discusses the linkage between APT and other local factors. The remaining section of this paper is organized as follows: Sect. 2 describes the data, statistical methods, and dynamic diagnostic approaches used in this study. Section 3 details the characteristics of the extreme heat event over the YRB in August 2022. Section 4 investigates the key local atmospheric factors and dynamical processes, the influence of upper-level atmospheric circulation on SAT, and the relationships among various local atmospheric variables. Section 5 examines the connection and relative contributions between local atmospheric dynamical processes and the diabatic heating from the land surface. Section 6 presents the conclusions and discussion.

2 Data and Method

2.1 Datasets

The 699 in-situ air temperature at 2-m height (T_{2m}) of 699 stations of China covering the period 1979–2022 from the National Meteorological Information Center of China is employed. Monthly and hourly reanalysis data on surface including T_{2m} and sea surface temperature (SST), and pressure levels including horizontal wind, vertical velocity, geopotential height (GHT) and air temperature are taken from the ERA5 reanalysis dataset on a $0.25° \times 0.25°$ grid (Hersbach et al. 2020). Since this study aims to figure out the key atmospheric processes of natural variability that resulted in this extreme heat event, all the data

used has been linearly detrended from the beginning to exclude the effect of global warming. The study area of the YRB is referred to as the 26°–33°N, 115°–122°E (the blue box in Fig. 1).

2.2 Statistical methods

2.2.1 Partial and semi-partial correlation analysis

Correlation analysis is used to analyze the linear relationship between series x and y, while x and y are usually affected by the third series z at the same time, the correlation coefficient may not fully reflect the linear relationship between x and y. Partial correlation analysis is to remove the influence of z from x and y, and then analyze the correlation between the remaining parts. Following Kim (2015), the partial correlation of x and y without the influence of z is

$$r_{x|z,y|z} = \frac{r_{x,y} - r_{x,z}r_{y,z}}{\sqrt{\left(1-r_{x,z}^2\right)\left(1-r_{y,z}^2\right)}}, \tag{1}$$

where $r_{x,y}$ $r_{x,z}$, and $r_{y,z}$ represent the correlation coefficients between x and y, between x and z, and between and y and z, respectively. Semi-partial correlation analysis is to only remove the influence of z from x (y), and then analyze the correlation between the remaining part and y (x). The semi-partial correlations of x and y given z are:

$$\begin{cases} r_{x|z,y} = \frac{r_{x,y} - r_{x,z}r_{y,z}}{\sqrt{1-r_{x,z}^2}} \\ r_{x,y|z} = \frac{r_{x,y} - r_{x,z}r_{y,z}}{\sqrt{1-r_{y,z}^2}} \end{cases}. \tag{2}$$

2.2.2 Effective degree of freedom

To avoid the effect of autocorrelation, we use the effective degrees of freedom N^* in the significance test of the coefficients of correlation, partial correlation, semi-partial correlation, and linear regression (Bretherton et al. 1999; Li et al. 2013).

$$N^* \approx \frac{N}{1+2\sum_{j=1}^{N-1}\frac{(N-j)}{N}\rho_x(j)\rho_y(j)}, \tag{3}$$

where N is the data length, $\rho_x(j)$ and $\rho_y(j)$ are the autocorrelation coefficients of time series x and y with a lag time of j, respectively.

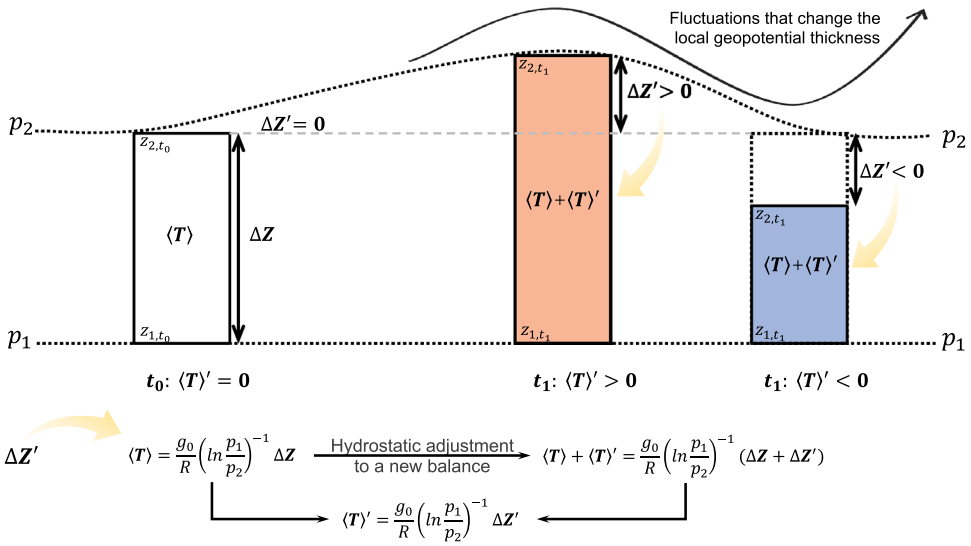

Fig. 2 Diagram of perturbation temperature adaptation to the perturbation geopotential thickness through hydrostatic adjustment. The geopotential thickness ($\Delta Z = Z_1 - Z_2$) of an air column bounded by two isobaric surfaces (p_1, p_2) and mean air temperature of the column ($\langle T \rangle$) are in balance ($\langle T \rangle = \frac{g_0}{R}\left(ln\frac{p_1}{p_2}\right)^{-1}\Delta Z$) at the moment t_0. When ΔZ is affected by external fluctuations and perturbation geopotential thickness ($\Delta Z'$) appears at the next moment t_1, $\langle T \rangle$ starts to adjust to $\Delta Z + \Delta Z'$. Thus, the perturbation air temperature ($\langle T \rangle'$) appears quickly and the new equilibrium state is achieved ($\langle T \rangle + \langle T \rangle' = \frac{g_0}{R}\left(ln\frac{p_1}{p_2}\right)^{-1}(\Delta Z + \Delta Z')$). Therefore, $\langle T \rangle'$ is proportional to $\Delta Z'$ ($\langle T \rangle' = \frac{g_0}{R}\left(ln\frac{p_1}{p_2}\right)^{-1}\Delta Z'$). For convenience, this diagram assumes that the geopotential height on the top of the column changes ($Z_{2,t_1} > Z_{2,t_0}$ or $Z_{2,t_1} < Z_{2,t_0}$) and the bottom remains unchanged ($Z_{1,t_1} = Z_{2,t_0}$). In fact, the variation of ΔZ is simultaneously determined by Z_1 and Z_2

2.2.3 Variance analysis

Variance describes the dispersion of data around its mean value, and is used to quantify the variability of a variable. To test whether there is a significant difference between the variability of two variables, the *F*-test is used. We set a null hypothesis that the variances of two series (s_1^2 and s_2^2) are the same. Then

$$F = \frac{\frac{n_1}{n_1-1}s_1^2}{\frac{n_2}{n_2-1}s_2^2}, \tag{4}$$

which follows the *F* distribution with the degree of freedom $N_1 = n_1 - 1, N_2 = n_2 - 1$, where n_1 and n_2 are the lengths of the two series. Given the significance level α, if $F \geq F_{\frac{\alpha}{2}}$, the null hypothesis is rejected (Hayashi 1982; Huang 1990).

2.2.4 Ranking Attribution Method (RAM)

To study this extreme heat event, we employ the RAM, which hypothesizes that extreme results are usually contributed by extreme factors (Sun et al. 2023). The RAM uses top/bottom ranks to mark possible extreme factors. For year *t* with a specific extreme event *Y* occurring, the RAM obtains the historical status of a relevant variable *X* at the year *t* by calculating the rank $R_{t(Y)}(X)$, where $X = \{x_i\}$, x_i ($i = 1,2, \cdots, n$) is a time series for ranking, *n* is the sample size (number of years). Positive (negative) ranks represent the ranking from the maximum (minimum), with 1 (–1) referring to the historical high (low).

In this study, we obtain the historical status of August mean T_{2m} in 2022 on every station (named as $R_{2022}(T_{2m})$ for short) through the RAM to verify the area where the heat extreme arose. To obtain as many as possible extreme contributors, the RAM is also used to search for the striking rankings ($R_{2022}(X)$) of relevant air-sea variables *X* on every spatial grid by the top (bottom) rankings. Last but not the least, physical connections between potential extreme factors are provided by other diagnostic methods to exclude pseudo contributors and establish responsible causality.

2.2.5 Local covariance and covariant factor

Covariance measures the average consistency of abnormal variations between two series *x* and *y*. For a single event, the sample size is 1,which is insufficient to capture the average consistency. Local covariance typically focuses on the interrelationship between two variables at a specific moment or within a short time window. Therefore, local covariance serves as a metric to quantify the consistency of two anomalies for a particular year in this study. The formula is as follow:

$$S_i = \left(x_i - \overline{x}\right)\left(y_i - \overline{y}\right), (i = 1, 2, \ldots, n), \tag{5}$$

where $\overline{x}$ and $\overline{y}$ are the mean values of two series.

Local covariance is a statistic with unit, which is not convenient to compare among multiple variables. Thus, the covariant factor between the two variables can be obtained by standardizing the original values and then calculating the local covariance. The formula of covariant factor is as follow:

$$S_i = \frac{(x_i-\overline{x})(y_i-\overline{y})}{\sigma_x \sigma_y}, (i = 1, 2, \ldots, n), \tag{6}$$

where σ_x and σ_y are the standard deviations of *x* and *y*, respectively. Greater absolute value of the covariant factor represents stronger consistency between changes of *x* and *y* at a specific moment.

2.2.6 Significance test for a single event

To rigorously test whether the relevant statistics in August 2022 are indeed significantly different from those in other years, we set a null hypothesis that the variable being tested (X_0) has the same true mean as those in other years (X_1, …, X_n). Let

$$\overline{X} = \sum_{i=1}^{n} X_i, \tag{7}$$

$$s^2 = \frac{1}{n}\sum_{i=1}^{n}\left(X_i - \overline{X}\right)^2, \tag{8}$$

$$t = \frac{X_0-\overline{X}}{s}\left(\frac{n-1}{n+1}\right)^{\frac{1}{2}}, \tag{9}$$

then *t* has a distribution of Student's *t* with *n*–1 degrees of freedom. This is a special case of significant test between the means of two samples where one sample contains only one value (Trenberth 1984).

2.3 Dynamical diagnosis

2.3.1 Perturbation hypsometric equation

According to the hypsometric equation, the geopotential thickness of the air column between two isobaric surfaces (p_1, p_2) is defined as follows (Holton and Hakim 2013):

$$\Delta Z = Z_2 - Z_1 = \frac{R\langle T\rangle}{g_0} ln\frac{p_1}{p_2}, \tag{10}$$

where $Z_1(Z_2)$ is the GHT at $p_1(p_2)$, ΔZ is the geopotential thickness between p_1 and p_2, g_0 is the gravitational acceleration and *R* is the gas constant for dry air. *T* is the air temperature with $\langle T\rangle$ indicating the mean value of the layer. We assume that the ΔZ and $\langle T\rangle$ of the column are in balance at the moment t_0 (Fig. 2):

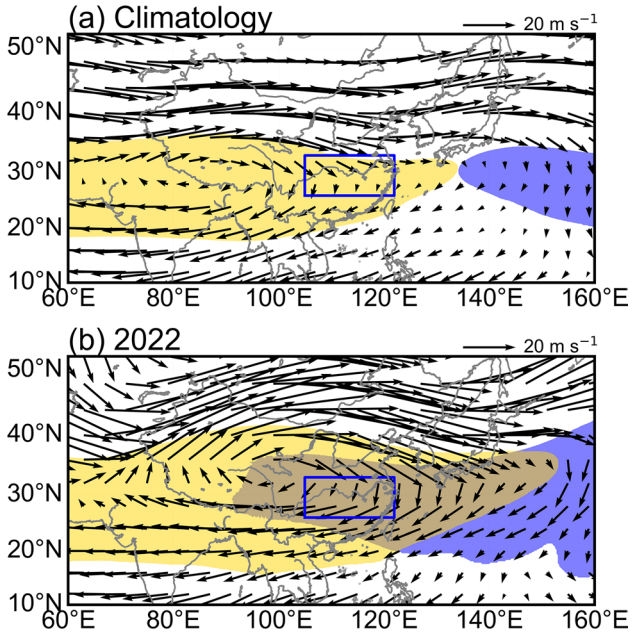

Fig. 3 **a** Climatological horizontal wind at 200 hPa (black vectors), the location of the South Asia High (yellow shading, indicated by the 12,500 gpm isolines at 200 hPa) and northwestern Pacific subtropical high (blue shading, indicated by the 5880 gpm isolines at 500 hPa) in August. **b** As in **a**, but for the results of August 2022

$$\langle T\rangle = \frac{g_0}{R}\left(ln\frac{p_1}{p_2}\right)^{-1}\Delta Z. \tag{11}$$

The perturbation hypsometric equation (Li et al. 2022) shows that ΔZ and $\langle T\rangle$ mutually adapt to each other. Changes in ΔZ lead to corresponding changes in mean temperature, and vice versa:

$$\langle T\rangle' = \frac{g_0}{R}\left(\ln\frac{p_1}{p_2}\right)^{-1}\Delta Z'. \tag{12}$$

with the $\langle T\rangle'$ and $\Delta Z'$ representing the deviations of $\langle T\rangle$ and APT from those at t_0. $\langle T\rangle'$ is proportional to $\Delta Z'$. When ΔZ is affected by external fluctuations, and $\Delta Z'$ appears, $\Delta Z + \Delta Z\prime$ are not in balance with $\langle T\rangle$. $\langle T\rangle$ starts to adjust to $\Delta Z + \Delta Z\prime$. Thus, $\langle T\rangle'$ occurs quickly at the next moment t_1:

$$\langle T\rangle + \langle T\rangle' = \frac{g_0}{R}\left(\ln\frac{p_1}{p_2}\right)^{-1}\left(\Delta Z + \Delta Z'\right) \tag{13}$$

Therefore, the fluctuations and imbalance phenomenon disappears, the field adaptation is completed, and a new equilibrium is formed. In this way, $\Delta Z'$can lead to $\langle T\rangle'$ through hydrostatic adjustment.

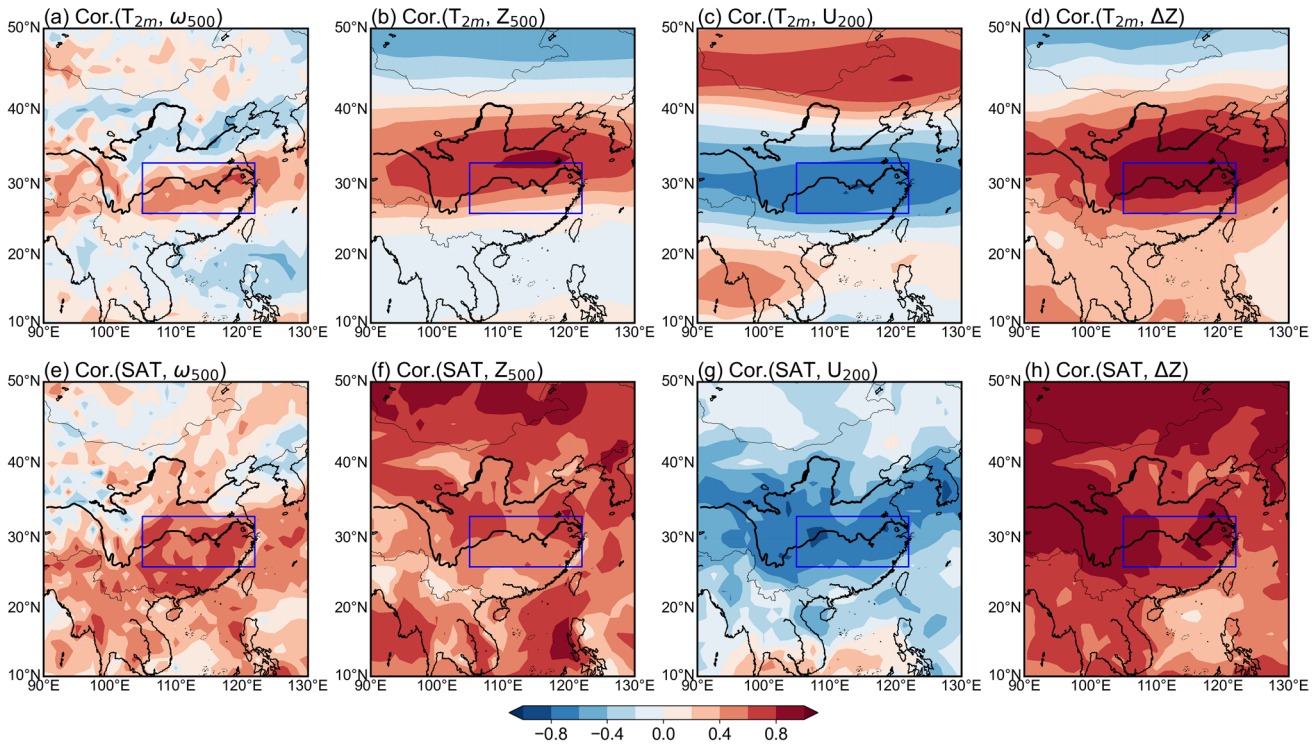

Fig. 4 **a** Spatial distribution of correlation coefficients between areal mean observed T_{2m} over the YRB and vertical motion at 500 hPa (ω_{500}) during 1979–2022 (shaded). **b–d** As in **a**, but for the geopotential height at 500 hPa (Z_{500}), zonal wind at 200 hPa (U_{200}) and geopotential thickness between 1000 and 500 hPa (ΔZ), respectively. **e** Correlation coefficients of surface air temperature (SAT) and ω_{500} at every spatial points in ERA5 reanalysis data (shaded). **f–h** As in **e**, but for the Z_{500}, U_{200} and ΔZ

2.3.2 Geopotential thickness tendency equation

The thermodynamic energy equation is as follow:

$$\frac{1}{\theta}\left(\frac{\partial\theta}{\partial t}+\boldsymbol{V}\bullet\nabla\theta+\omega\frac{\partial\theta}{\partial p}\right)=\frac{1}{c_pT}\frac{dQ}{dt}, \tag{14}$$

with θ, $\boldsymbol{V}$, ω, T and Q indicating the potential temperature, horizontal wind, vertical velocity in p-coordinate, air temperature, and diabatic heating of air. c_p is the isobaric specific heat of the air. After considering the quasi-geostrophic approximation and quasi-static equilibrium,

$$\frac{\partial\phi}{\partial p}=-\frac{1}{\rho}, \tag{15}$$

with ϕ and ρ representing the geopotential and air density. Equation (14) can be expressed as

$$\frac{\partial}{\partial t}\frac{\partial\phi}{\partial p}=-\boldsymbol{V_g}\bullet\nabla\frac{\partial\phi}{\partial p}-\sigma\omega-\frac{R}{c_pp}\frac{dQ}{dt}, \tag{16}$$

where $\boldsymbol{V_g}$ is the geostrophic winds and σ is the static stability of atmosphere:

$$\sigma=-\frac{1}{\rho\theta}\frac{\partial\theta}{\partial p}. \tag{17}$$

We may integrate Eq. (16) from pressure level p_1 to level p_2 ($p_1>p_2$) to get

$$\frac{1}{g}\frac{\partial(\phi_1-\phi_2)}{\partial t}=\frac{1}{g}\int_{p1}^{p_2}\boldsymbol{V_g}\bullet\nabla\frac{\partial\phi}{\partial p}dp+\frac{1}{g}\int_{p1}^{p_2}\sigma\omega dp+\frac{1}{g}\int_{p1}^{p_2}\frac{R}{c_pp}\frac{dQ}{dt}dp. \tag{18}$$

Let $\{\}=\frac{1}{g}\int_{p_1}^{p_2}\bullet\,dp$, we can rewrite Eq. (18) as

$$\frac{\partial(\Delta Z)}{\partial t}=\left\{\boldsymbol{V_g}\bullet\nabla\frac{\partial\phi}{\partial p}\right\}+\{\sigma\omega\}+\left\{\frac{R}{c_pp}\frac{dQ}{dt}\right\}. \tag{19}$$

The tendency of ΔZ depends on three terms, including the horizontal advection of vertical geopotential shear (H_{ADV}), the process relevant to air vertical motion and atmosphere static stability (V_ω), and the diabatic heating within the column between p_1 and p_2. In the stable atmosphere, $\frac{\partial\theta}{\partial p}<0$, and $\sigma>0$, thus sign of V_ω depends on that of ω.

3 Heat extreme over the YRB in August 2022

In August 2022, the monthly averaged T_{2m} over the YRB reached unprecedented extremes. Spatial distribution of observed anomalous T_{2m} shows that the anomalies are 3–4 °C above normal (Fig. 1a). Rankings of August T_{2m} in 2022 show that most stations record their highest temperatures since 1979 (deep red dots in Fig. 1c). After removing the long-term linear trend to mitigate the effects of global warming, both observation and ERA5 data reveal that the regionally averaged T_{2m} anomaly over the YRB is also exceptionally high in 2022 (Fig. 1b), with a correlation coefficient of 0.99 between the two datasets. This suggests that using ERA5 reanalysis data to diagnose variation of observed T_{2m} in this region is reasonable and feasible. Furthermore, the observed T_{2m} is highly correlated with the local mean temperature of the air column between 1000 and 500 hPa isobaric surfaces, achieving a correlation coefficient of 0.96 (Fig. 1d). The mean temperature of the air column is also extreme in 2022, as T_{2m} is a component of the column-mean temperature, and their variations are synchronous. Therefore, the variation of the column-mean temperature can largely represent the variation of T_{2m}.

Existing researches have demonstrated that multiple local atmospheric factors can influence the T_{2m} through various atmospheric dynamical processes (He et al. 2023; Hua et al. 2023; Tang et al. 2023; Wang et al. 2023; Zhang et al. 2023b; Gong et al. 2024; Huang et al. 2024; Liao et al. 2024; Yuan et al. 2024). These factors are local GHT at 500 hPa (Z_{500}), vertical velocity at 500 hPa (ω_{500}), and zonal wind at 200 hPa (U_{200}). Since the atmospheric dynamical processes related to these factors are induced by large-scale atmospheric circulation systems including the NWPSH and the South Asia high (SAH).

Table 1 Relationships between anomalous T_{2m} over the YRB and relevant local atmospheric variables, including anomalous atmospheric geopotential thickness between 1000 and 500 hPa (ΔZ), geopotential height at 500 hPa (Z_{500}), zonal wind at 200 hPa (U_{200}), and vertical velocity at 500 hPa (ω_{500}), and connections between these local variables

Series 1	Series 2	Correlation coefficient	Explained variance (%)
ΔZ	T_{2m}	0.88^{**}	77.8
Z_{500}	T_{2m}	0.61^{**}	37.0
U_{200}	T_{2m}	-0.80^{**}	64.3
ω_{500}	T_{2m}	0.73^{**}	53.2
$\Delta Z\|Z_{500}$	T_{2m}	0.64^{**}	40.8
$\Delta Z\|U_{200}$	T_{2m}	0.39^{**}	15.2
$\Delta Z\|\omega_{500}$	T_{2m}	0.58^{**}	33.6
$Z_{500}\|\Delta Z$	T_{2m}	0.03	0
$U_{200}\|\Delta Z$	T_{2m}	–0.14	1.9
$\omega_{500}\|\Delta Z$	T_{2m}	0.32^{*}	10.2
ω_{500}	$T_{2m}\|\Delta Z$	0.58^{**}	33.6
$(\Delta Z, \omega_{500})$	T_{2m}	0.94^{**}	88.1

Note. These values are correlation coefficients between two local area-mean series (Series 1 and Series 2) and the percentage that the variance of Series 2 can be explained by Series 1. "$A|C$" means subtracting the influence of C on A when analyzing the relationship between A and B. "(A, C, D)" means calculating multiple correlation coefficient with B. The correlation coefficients with * and ** represent the statistical significance above 95% and 99% confidence level, respectively. The same here in after

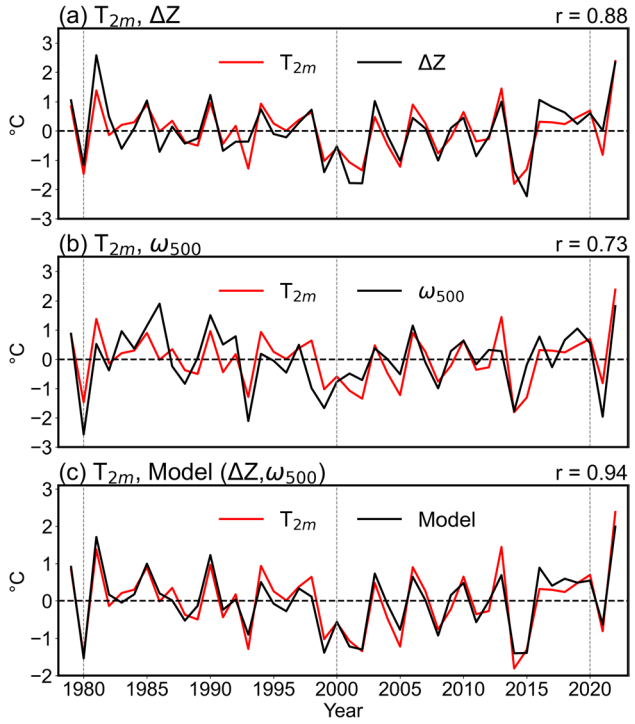

Fig. 5 **a–c** Time series of areal mean anomalies in the YRB for observed T_{2m} (red lines, ℃). **a** Standardized ΔZ (black line), **b** ω_{500} (black line), and **c** the model established by ΔZ and ω_{500} (black line) from ERA5. The values in the upper right represent correlation coefficients between corresponding two time series

As shown in Fig. 3, we used the 12,500 (5880) gpm isolines at 200 (500) hPa to identify the location of the SAH and NWPSH (Wei et al. 2015; Wang et al. 2023). In climatology, the August SAH and NWPSH locate over the continent of Asia and northwestern Pacific, respectively. With the center of the SAH lying over the Tibet Plateau, due to the geostrophic equilibrium, the westerly winds dominate over the YRB (Fig. 3a). In August 2022, The SAH (NWPSH) strengthened and expanded eastward (westward), with the middle and upper-level high-pressure systems overlap above the YRB (Fig. 3b). Meanwhile, the northeastward movement of the SAH center led to the upper-level east winds over the YRB. These large-scale atmospheric anomalies of August 2022 are consistent with the results in previous studies (He et al. 2023; Hua et al. 2023; Tang et al. 2023; Wang et al. 2023; Zhang et al. 2023b; Gong et al. 2024; Huang et al. 2024; Liao et al. 2024; Yuan et al. 2024).

The direct linkages between large-scale systems and T_{2m} over the YRB needs to be confirmed. As shown in Fig. 4a–c, the spatial distributions of correlation coefficients between the areal mean T_{2m} over the YRB and the above three variables show that maximums are all distributed over or adjacent to the study area. The point-to-point correlation analysis also shows that the SAT over the YRB is highly correlated with the local variables above it (Fig. 4e–g).

The above results indicate that the relevant large-scale atmospheric circulations affect the T_{2m} by directly influencing the atmospheric dynamic processes over the local or adjacent area of the study area (the blue rectangle). In order to unify the calculation processes, the analysis of local atmospheric dynamic factors in this paper are based on the study area. The time series of local factors is obtained by the areal mean values over the study area. Based on the atmospheric hydrostatic adjustment processes (Ye and Li 1965; Li et al. 2022), this study proposes to take the APT between 1000 and 500 hPa isobaric surfaces ($\Delta Z_{1000-500}$, take ΔZ for short) as a local atmospheric factor to explain the variation of August T_{2m} over the YRB. Figure 4d shows that the ΔZ over the study area and its northern neighboring areas is highly correlated with the T_{2m} over the study area. The SAT at each space point is highly correlated with the ΔZ above it (Fig. 4h). The perturbation hypsometric equation (Li et al. 2022) shows that when ΔZ is affected by external fluctuations, T_{2m} increases or decreases according to the change of ΔZ through hydrostatic adjustment process to achieve a new equilibrium state (Fig. 2). Therefore, ΔZ is likely to be one of the key local atmospheric dynamic factors for the interannual variation of T_{2m} over the YRB in August.

4 Key local atmospheric dynamic processes

4.1 Essential effect of atmospheric local geopotential thickness and vertical motion

To better understand the increase of T_{2m} and improve its prediction skill, it is crucial to identify the key local atmospheric factors and processes. Table 1 shows that the variation of ΔZ is the most strongly correlated with variation of T_{2m} compared to the other three factors (Z_{500}, ω_{500}, and U_{200}), with a correlation coefficient of 0.88, which explains 77.8% of the variance in T_{2m}. The results coincident with the conclusion in Thompson and Wallace (1998), which shows that ΔZ anomalies bear a stronger resemblance to the T_{2m} anomalies in the panel below in the Northern Hemisphere when compared with Z_{500}.

To further clarify the relationship between ΔZ and the above mentioned three factors in influencing T_{2m}, we employed semi-partial correlation (Eq. 2) to isolate the effects of each factor on the others and examined the relationship between the remaining component and T_{2m} (Table 1). The results show that after removing the influences of Z_{500}, ω_{500}, and U_{200} from ΔZ, the correlation between ΔZ and T_{2m} remains significant, exceeding the 99%

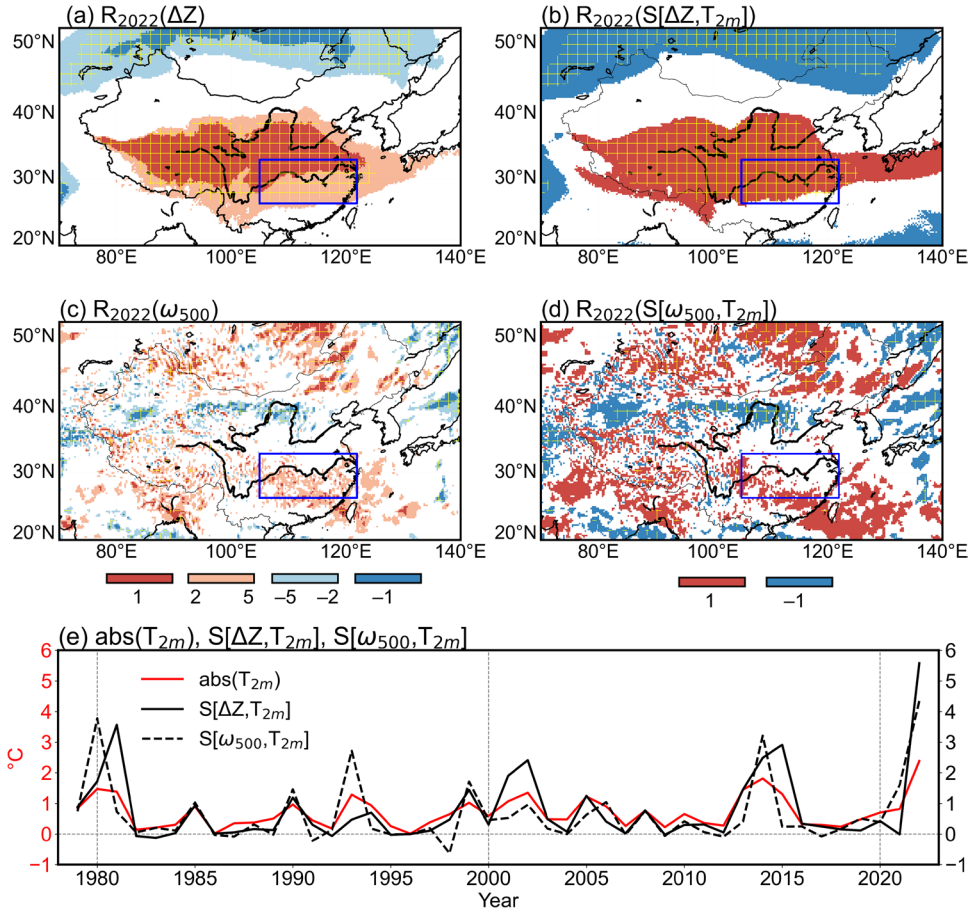

Fig. 6 **a** Ranking of August ΔZ (shaded) in 2022 since 1979. **b** As in **a**, but for local covariance between ΔZ and areal mean T_{2m} anomaly over the YRB (S[ΔZ,T_{2m}]) in 2022. **c** As in **a**, but for ω_{500}. **d** As in **b**, but for ω_{500}. The yellow cross-hatched areas in **a**–**d** indicate statistical significance of abnormal ΔZ or ω_{500} at the 95% confidence level. **e** Time series of absolute value of areal mean T_{2m} anomaly (red line, ℃), standardized areal mean S[ΔZ,T_{2m}] (black solid line) and S[ω_{500},T_{2m}] (black dashed line) over the YRB

confidence level. This indicates that the correlation between ΔZ and T_{2m} is not dominated by other factors. However, when the influence of ΔZ is removed from Z_{500} and U_{200}, the correlation between Z_{500} and U_{200} with T_{2m} disappears, with the explained variance approaching zero. This suggests that ΔZ encompasses information from both Z_{500} and U_{200}, allowing ΔZ to effectively substitute for Z_{500} and U_{200} in influencing T_{2m}.

It is noteworthy that ω_{500} still shows a significant correlation with T_{2m} after removing the influence of ΔZ, with a confidence level exceeding 95% (Table 1). For the portion of T_{2m} variation unexplained by ΔZ, ω_{500} can account for 33.6% of its variance. The multiple correlation coefficient between ΔZ, ω_{500}, and T_{2m} reaches 0.94, allowing for an explanation of up to 88.1% of the interannual variation of T_{2m}. Thus, ΔZ is the most critical atmospheric factor influencing the interannual variation of August T_{2m} over the YRB, while the role of ω_{500} should not be overlooked. Notably, T_{2m} reached its maximum in 2022, whereas neither ΔZ nor ω_{500} peaked in that year (Fig. 5a and b). However, the linear model established for T_{2m} based on ΔZ and ω_{500} reached its maximum in 2022 (Fig. 5c). Therefore, both ΔZ and ω_{500} should be considered as key local atmospheric factors in analyzing interannual variation of T_{2m} as well as in explaining extreme event in 2022.

For the extreme heat event in August 2022, both ΔZ and ω_{500} over the YRB exhibited significant differences compared to other years (yellow cross-hatched areas in Fig. 6a and b). The spatial distribution of ΔZ rankings in 2022 shows that the ΔZ in the northern (southern) part of the YRB was historically high (ranked among the historical top five)(Fig. 6a). ω_{500} also ranked among the historical top five (Fig. 6c). The local covariance between ΔZ (ω_{500}) and T_{2m} reflects the strength of their variability consistency in a certain year (Eq. 5). Greater absolute value of the local covariance means stronger consistency of variability between the two variables. Over the YRB, the local covariance between ΔZ and T_{2m} in 2022 was historically high (Fig. 6b), while the local covariance between ω_{500} and T_{2m} in 2022 exhibited no spatially organized pattern (Fig. 6d). The covariant factors are the standardized local covariances, whose absolute values also represent the strength of variability consistency between the two variables in a certain year and allow for comparisons among different variables (Eq. 6). The covariant factor between ΔZ (ω_{500}) and T_{2m} reached their maximum in 2022, but the covariant factor of ΔZ was greater than that of ω_{500} in 2022 (Fig. 6e). Thus, the extreme heat event in 2022 was directly driven by the local ΔZ, with ω_{500} playing a secondary role.

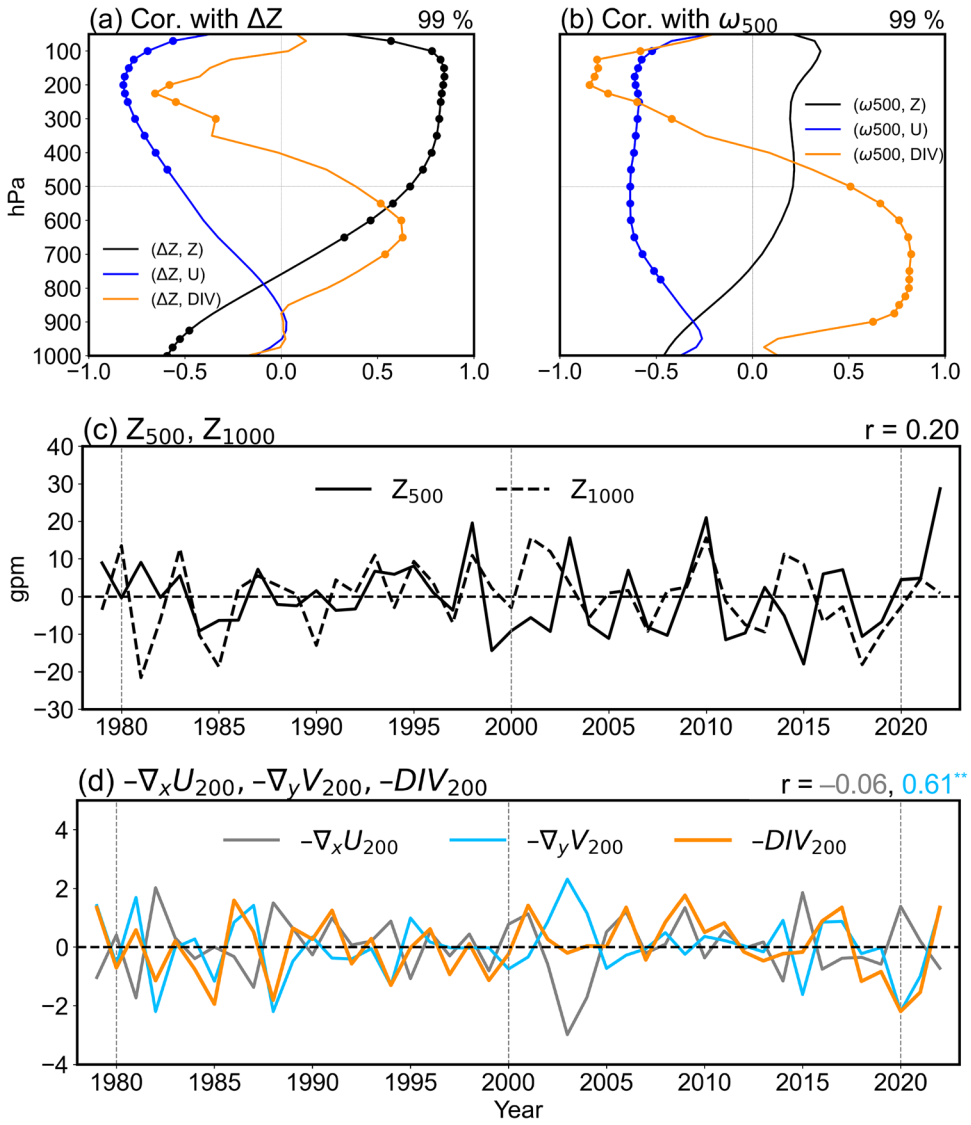

Fig. 7 **a** Correlation coefficients between August areal mean ΔZ and areal mean geopotential height (black line), zonal wind (blue line) and horizontal wind divergence (orange line) on different pressure levels. **b** Same as **a** but for areal mean ω_{500}. The dotted in **a** and **b** indicates that the statistical significance exceeds 99% confidence level. **c** Time series of areal mean geopotential height anomaly at 500 hPa (Z_{500}, solid line, gpm) and 1000 hPa (Z_{1000}, dashed line, gpm) over the YRB. **d** Time series of areal mean zonal gradient of U_{200} multiplied by –1 ($-\nabla_x U_{200}$, gray line), meridional gradient of meridional wind (V_{200}) multiplied by –1 ($-\nabla_y V_{200}$, blue line) and horizontal wind divergence (orange line) at 200 hPa (DIV_{200}) multiplied by –1. The value in the upper right of **c** represents correlation coefficient between Z_{500} and Z_{1000}. The gray (blue) value in the upper right of **d** represents correlation coefficient between DIV_{200} and zonal gradient of U_{200} (meridional gradient of V_{200}), with ** representing above 99% confidence level

Table 2 Connections between T_{2m} and high-level atmosphere, including geopotential height (Z_{200}), zonal wind (U_{200}), and horizontal divergence (DIV_{200}) at 200 hPa

Series 1	Series 2	Correlation coefficient	Explained variance (%)
Z_{200}	T_{2m}	0.61**	37.2
U_{200}	T_{2m}	–0.80**	64.3
DIV_{200}	T_{2m}	–0.67**	44.9
$Z_{200}\|\Delta Z$	T_{2m}	–0.23	5.3
$Z_{200}\|\omega_{500}$	T_{2m}	0.45*	20.3
$U_{200}\|\Delta Z$	T_{2m}	–0.14	1.9
$U_{200}\|\omega_{500}$	T_{2m}	–0.45*	20.1
$DIV_{200}\|\Delta Z$	T_{2m}	–0.17	2.9
$DIV_{200}\|\omega_{500}$	T_{2m}	–0.07	0.5

4.2 Influence of local upper-level circulation on surface air temperature

After identifying the key local atmospheric factors as ΔZ and ω_{500}, we further explore the relationships between other local variables and ΔZ (ω_{500}). Figure 7a presents the correlation coefficients between ΔZ and the local GHT, zonal wind, and horizontal divergence at various pressure levels. The results show that an increase in ΔZ is significantly relevant to an increase in GHT at 600–100 hPa, while it is also significantly correlated with a decrease in GHT at 1000–900 hPa. Thus, ΔZ is determined by the GHTs in both the upper and lower atmosphere layers.

Previous studies regarded changes in GHT at 500 hPa can largely represent the changes in air column thickness between 1000 and 500 hPa (Wallace et al. 1993; Rousta et al. 2019; Dubey and Kumar 2023), since they are strongly correlated with each other, which indicates that variations in

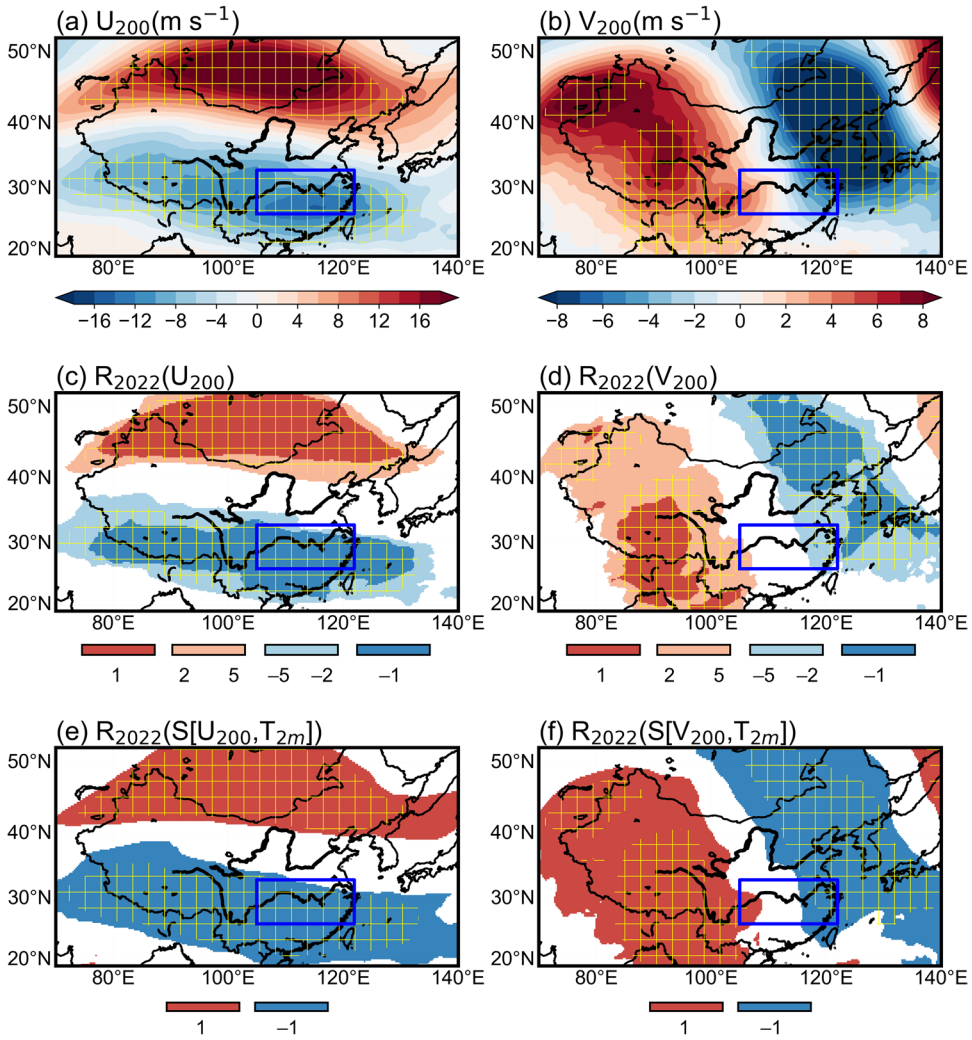

Fig. 8 **a** Anomalous August U_{200} (shaded, m s^{-1}) in 2022. **b** As in **a**, but for V_{200}. **c** Ranking of August U_{200} (shaded) in 2022 since 1979. **d** As in **c**, but for V_{200}. **e** As in **c**, but for the local covariance between U_{200} and areal mean T_{2m} anomaly over the YRB (S[U_{200},T_{2m}]). **f** As in **e**, but for V_{200}. The yellow cross-hatched area indicates statistical significance of U_{200} or V_{200} anomalies at the 95% confidence level

GHT at 1000 hPa are relatively small and can be disregarded to some extent. Figure 7c is the time series of regionally averaged GHT at 500 hPa and 1000 hPa over the YRB, with a correlation coefficient of 0.2, indicating no significant linkages. When using the range to measure variation, the ranges for the time series of GHT at 500 hPa and 1000 hPa are 457.0 gpm and 364.2 gpm, respectively, with the standard deviations of 95.5 gpm and 88.2 gpm. The variance analysis (Eq. 4) shows no significant difference in the variances between the two series, which indicates that the variations in GHT at 1000 hPa can not be neglected. Therefore, the advantage of using ΔZ lies in its ability to incorporate information from both the upper and lower levels of atmosphere, which provides a more accurate reflection of changes in the APT. In August 2022, the increase in ΔZ primarily originates from an extreme rise in the GHT at 500 hPa, while the GHT at 1000 hPa exhibited no significant anomalies (Fig. 7c). In addition, ΔZ is highly correlated with the zonal wind at 200 hPa, with the correlation coefficient reaching –0.82. The increase of ΔZ is also significantly associated with upper-level convergence and lower-level divergence.

Figure 7b shows the correlation coefficients between ω_{500} and GHT, zonal wind, and horizontal divergence at various pressure levels. The results indicate that ω_{500} is uncorrelated with the GHT from 1000 to 100 hPa, suggesting that Z_{500} can not adequately explain the variations in ω_{500}. While ω_{500} is significantly correlated with the mid- to upper-level zonal wind, the correlation is not as strong as that between ΔZ and zonal wind. Additionally, positive ω_{500} anomaly is highly correlated with the upper-level convergence and lower-level divergence, with correlation coefficients reaching 0.82 and 0.85, respectively. This relationship is primarily determined by the continuity of air and the conservation of mass in the entire atmospheric column.

The upper atmospheric circulation, represented by variables at 200 hPa, is not only closely linked to ΔZ and ω_{500}, but also exhibits a significant correlation with T_{2m} (Table 2). The correlation coefficients for GHT at 200 hPa (Z_{200}), zonal

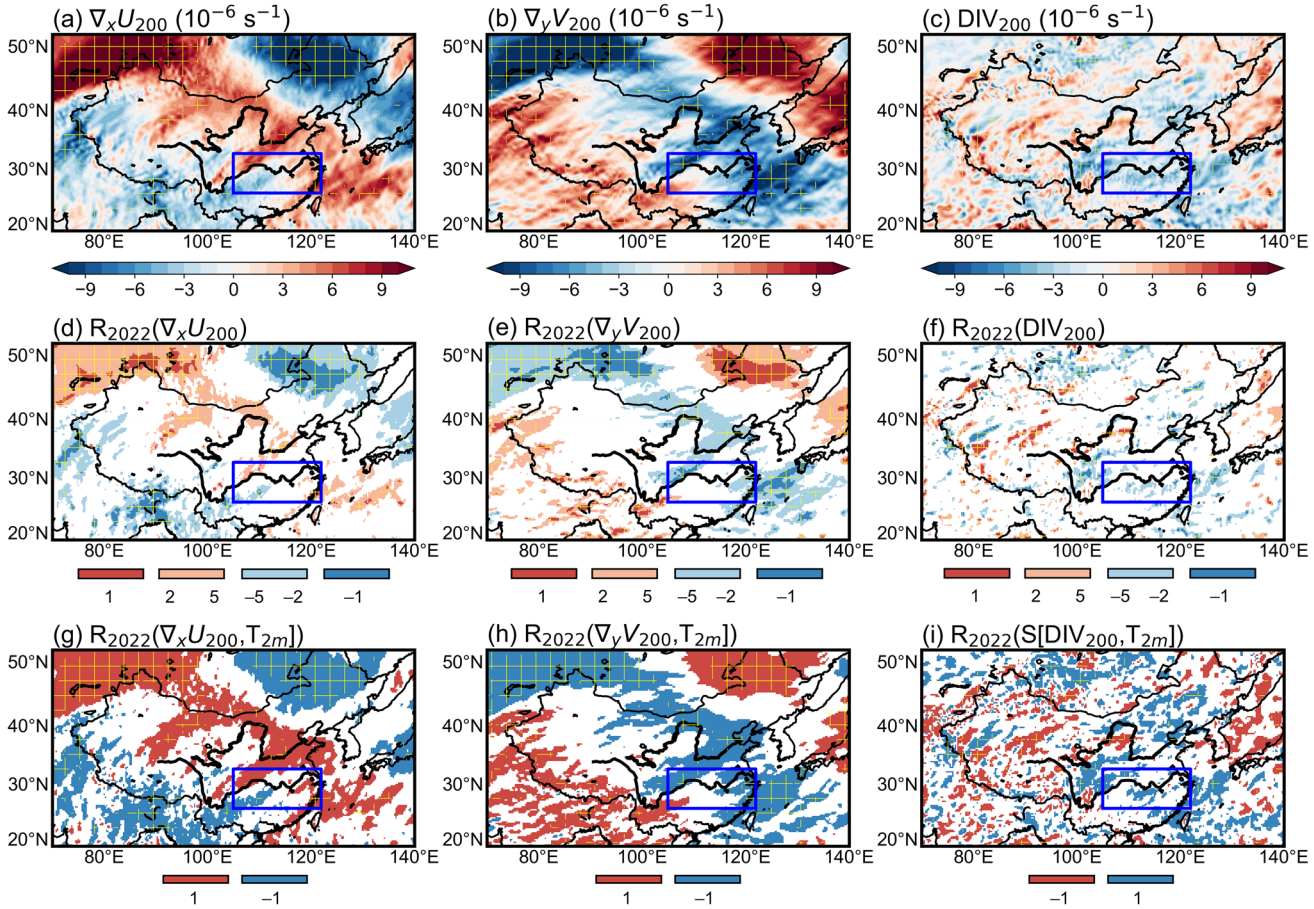

Fig. 9 **a** Anomalous August zonal gradient of U_{200} (shaded, 10^{-6} s^{-1}) in 2022. **b** As in **a**, but for meridional gradient of V_{200}. **c** As in **a**, but for DIV_{200}. **d** Ranking of August zonal gradient of U_{200} in 2022 since 1979 (shaded). **e** As in **d**, but for meridional gradient of V_{200}. **f** As in **d**, but for DIV_{200}. **g** As in **d**, but for the local covariance between zonal gradient of U_{200} and areal mean T_{2m} anomaly over the YRB ($S[U_{200},T_{2m}]$) (shaded). **h** As in **g**, but for meridional gradient of V_{200}. **i** As in **g**, but for DIV_{200}. The yellow cross-hatched area indicates statistical significance of anomalies at the 95% confidence level

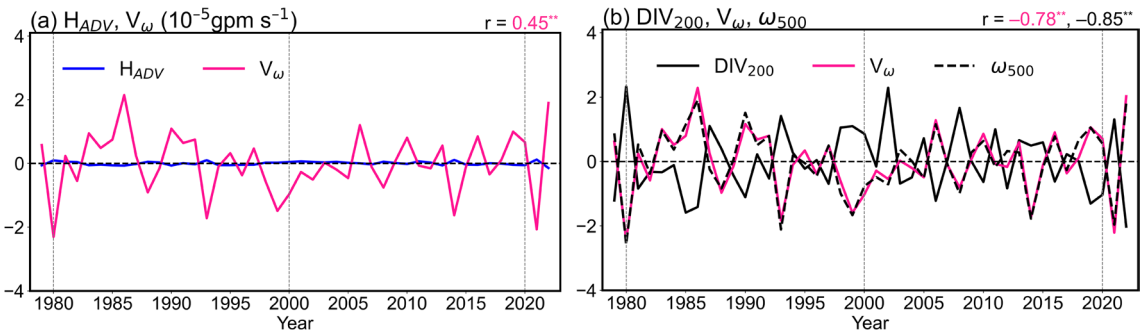

Fig. 10 Time series of areal mean anomalies over the YRB. **a** The horizontal advection of vertical geopotential shear (H_{ADV}, blue line) and product of air vertical motion and atmosphere static stability (V_ω, pink line) between 1000 and 500 hPa in the geopotential thickness tendency equation, which are calculated based on the hourly data of ERA5 and then averaged monthly. **b** Standardized DIV_{200} (black solid line), V_ω(pink line), and vertical velocity at 500 hPa (black dashed line). The value in the upper right of **a** represents correlation coefficients between ΔZ and V_ω. The values in the upper right of **b** represent correlation coefficients of V_ω (in pink) and ω_{500} (in black) with DIV_{200}. The values with ** representing above 99% confidence level

wind at 200 hPa (U_{200}), and horizontal wind divergence at 200 hPa (DIV_{200}) with T_{2m} are 0.61, –0.80, and –0.67, respectively. This indicates that an increase in Z_{200}, along with anomalous easterly winds and horizontal wind convergence, is associated with rising T_{2m}. How does the upper-level circulation influence T_{2m}? Through semi-partial correlation analysis, we found that when the component related to ΔZ is removed from the Z_{200}, U_{200}, and DIV_{200} series, their significance with T_{2m} disappears. When the component related to ω_{500} is removed from these series, the confidence level of the correlation coefficients for Z_{200} and U_{200} with T_{2m} drops from 99 to 95%. The correlation coefficient for DIV_{200} with T_{2m} becomes –0.07 after removing the influence of ω_{500}. These results suggest that the relationships between high-level circulations and T_{2m} cannot be established without the involvement of ΔZ and ω_{500}. Thus, ΔZ and ω_{500} serve as crucial bridges through which upper-level atmospheric circulation affects T_{2m}.

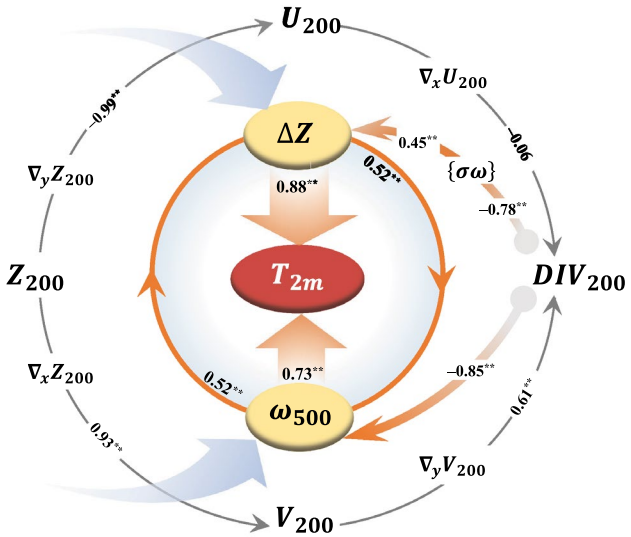

Fig. 11 The dynamic processes that high-level atmosphere affects the T_{2m}. The T_{2m} is directly affected by ΔZ and ω_{500}, with ΔZ and ω_{500} interacting with each other. The meridional (zonal) gradient of geopotential height ($\nabla_y Z_{200}$,$\nabla_x Z_{200}$) is highly correlated with zonal (meridional) wind at higher atmosphere (U_{200}, V_{200}, take 200 hPa for example). The meridional gradient of meridional wind ($\nabla_y V_{200}$) induces horizontal wind convergence at 200 hPa (DIV_{200}), which is conducive to the downward motion at mid-lower atmosphere (ω_{500}). According to the geopotential thickness tendency equation, the downward motion from 1000 to 500 hPa ($\{\sigma\omega\}$) favors the increase of ΔZ. Thus, the anomalous positive geopotential height at high-level atmosphere makes the T_{2m} higher by thickening the air column between 1000 and 500 hPa and intensifies downward motion at 500 hPa. The values are correlation coefficients between two variables at start point and end point of arrows, with ** representing above 99% confidence level. The two blue vectors indicate other factors that relevant to ΔZ and ω_{500}, respectively

4.3 Linkages among local upper-level geopotential height, horizontal wind, and divergence

The above results indicate that local Z_{200}, U_{200}, and DIV_{200} indirectly affect T_{2m} by influencing ΔZ and ω_{500}. In analyzing the mechanisms by which upper-level atmospheric circulation impact ΔZ and ω_{500}, we should first clarify the relationships among Z_{200}, U_{200}, and DIV_{200}. The quasi-geostrophic balance exists between Z_{200} and the horizontal wind field. Over the study area, the areal mean U_{200} is highly correlated with the areal mean meridional gradient of Z_{200}, with a correlation coefficient of –0.99. The areal mean meridional wind (V_{200}) is highly correlated with the areal mean zonal gradient of Z_{200}, with a correlation coefficient of 0.93.

Figure 8 presents the anomalies and rankings of the horizontal wind. The anomalous U_{200} also reached historical extremes (Fig. 8a, c, and e), this is due to that the YRB located at the southern edge of abnormal South Asian high, which reached an unprecedented strength in August 2022 (He et al. 2023; Zhang et al. 2023b). Additionally, there are abnormal northerly and southerly winds at the eastern and western sides of the YRB, respectively (Figs. 8b, d, and f). The regionally averaged southerly and northerly winds canceled each other out, resulting in no significant correlation between the regionally averaged V_{200} and T_{2m}.

Figures 8a and b show that the anomalies in U_{200} and V_{200} are not uniform within the YRB region in August 2022. The anomalous easterly winds are the strongest at the center of the study area, while the southerly wind anomalies on the west side weaken with latitude. Conversely, the anomalous northerly winds on the eastern side strengthen with latitude. The DIV_{200} is essentially induced by the ageostrophic wind, while it is plainly influenced by the meridional gradient of V_{200} and the zonal gradient of U_{200} from the perspective of local variables. The unevenness of the anomalous easterly winds within the study area causes horizontal wind divergence (Fig. 9a, d, and g), while the inhomogeneity of the anomalous V_{200} results in anomalous horizontal wind convergence (Fig. 9b, e, and h). Thus, the anomalous convergence of upper-level horizontal winds over the YRB is primarily driven by the spatial unevenness of the anomalous meridional wind (Fig. 9c, f, and i). Furthermore, DIV_{200} reached a strong local covariance with T_{2m} in 2022. Analysis of multi-year regionally averaged series in August results in similar conclusions. The anomalous convergence of upper-level horizontal winds over the YRB is not related to the anomalous zonal gradient of U_{200}, but is mainly determined by the anomalous meridional gradient of V_{200}, with a correlation coefficient of 0.61, exceeding 99% confidence level (Fig. 7d).

Thus, we can summarize the relationships among Z_{200}, U_{200}, V_{200}, and DIV_{200} over the YRB in August 2022. Influenced by the southern edge of the extremely intensified

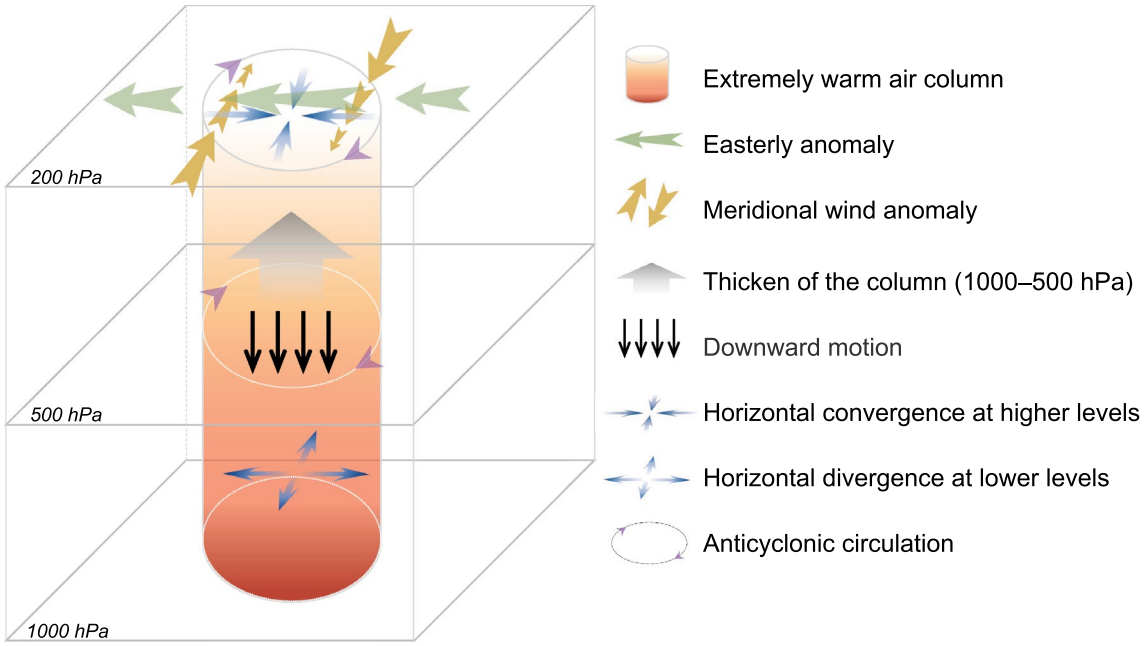

Fig. 12 Diagram of local atmosphere dynamic process on influencing T_{2m} over the YRB in August 2022

Table 3 Relationships between ΔZ, ω_{500} and diabatic heating relevant to the land surface, including net downward shortwave radiation (*SR*), net upward longwave radiation (*LR*), net upward latent heat flux (*LHF*), and net upward sensible heat flux (*SHF*)

Series 1	Series 2	Correlation coefficient	Explained variance (%)
SR	T_{2m}	0.80^{**}	64.7
LR	T_{2m}	0.63^{**}	39.2
LHF	T_{2m}	0.72^{**}	51.2
SHF	T_{2m}	0.71^{**}	50.6
$LR + LHF + SHF$	T_{2m}	0.79^{**}	62.4
SR	$LR + LHF + SHF$	0.99^{**}	99.7
$SR \vert \omega_{500}$	T_{2m}	0.33	10.8
$\omega_{500} \vert SR$	T_{2m}	0	0
$SR \vert \Delta Z$	T_{2m}	0.41^{**}	17.1
$\Delta Z \vert SR$	T_{2m}	0.55^{**}	30.2
$(\Delta Z, \omega_{500})$	T_{2m}	0.94^{**}	88.1
$(\Delta Z, \omega_{500}, SR)$	T_{2m}	0.98^{**}	95.8

South Asian high and the effect of quasi-geostrophic adjustment, U_{200} and V_{200} adjust to Z_{200}, leading to the dominance of extreme easterly winds within the study area. The eastern (western) side of the YRB is controlled by anomalous northerly (southerly) winds. The meridional gradient of V_{200} determines DIV_{200}. The anomalous northerly winds on the eastern side increase with latitude and the anomalous southerly winds on the western side decrease with latitude, which results in strong upper-level convergence.

4.4 The mechanism of air column thickness variations

The air column in this study is defined with the upper boundary at 500 hPa and the lower boundary at 1000 hPa, yet the variation in ΔZ exhibits the strongest correlation with the GHT at 200 hPa, with a correlation coefficient of 0.85 (Fig. 7a). Therefore, the mechanism underlying the thickening of the air column and its relationship with the upper-level atmospheric circulation are intriguing questions. To address these questions, we vertically integrated the thermodynamic energy equation to derive the tendency equation of ΔZ (Eq. 19). This equation reveals that the ΔZ between two isobaric surfaces is determined by three components: the horizontal advection of vertical geopotential shear (H_{ADV}), the process relevant to air vertical motion and atmosphere static stability (V_{ω}), and the diabatic heating within the column.

Figures 10a presents the time series of the regionally averaged anomalous H_{ADV} and V_{ω} within the 1000–500 hPa air column over the YRB. The anomalous values of H_{ADV} and V_{ω}, which were calculated based on the hourly data of ERA5 and then averaged monthly, show that the correlation coefficients between V_{ω} and ΔZ is 0.45, which exceeds the 99% confidence level. Notably, anomalous H_{ADV} nears zero, indicating that the thickening of the air column over the YRB in August is primarily attributed to the positive contributions from V_{ω} and diabatic heating. In the V_{ω}, σ is positive, indicating that downward motion within the air column contributes to its thickening. Figure 10b shows that DIV_{200}

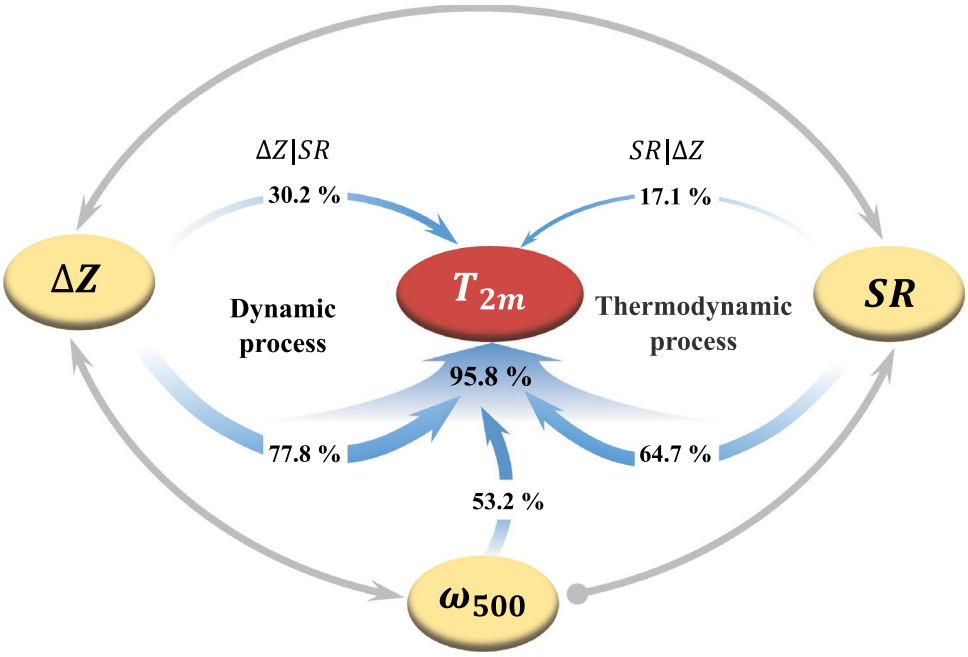

Fig. 13 Linkages between the local atmosphere dynamic and thermodynamic processes. ΔZ and shortwave radiation (SR) increase the T_{2m} through dynamic and thermodynamic processes, which can explain 77.8% and 64.7% of the variance in T_{2m}, respectively. ω_{500} is closely related to the two processes through thickening the air column to increase ΔZ and reducing the cloud cover to increase SR. There is also an interaction between ΔZ and SR, which is a positive feedback process. After ΔZ and SR remove the influence of each other, their contributions on T_{2m} remains 30.2% and 17.1%, respectively. ΔZ, ω_{500}, and SR can explain 95.8% of the variance in T_{2m}

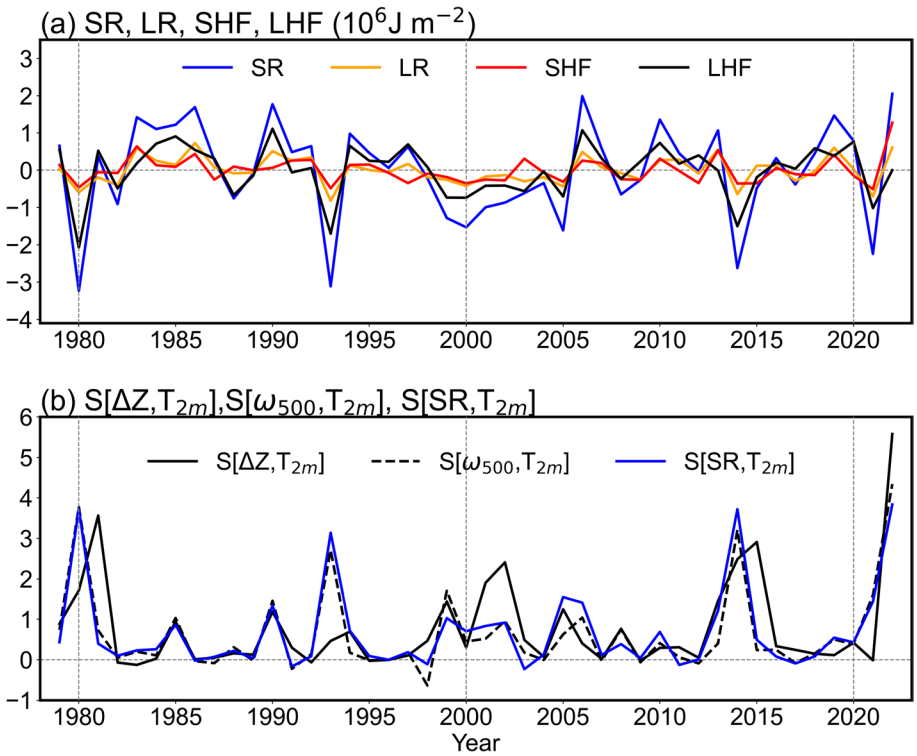

Fig. 14 **a** Time series of areal mean net downward shortwave radiation (SR, blue line), net upward longwave radiation (LR, orange line), net upward sensible heat flux (SHF, red line), and net upward latent heat flux (LHF, black line). **b** Time series of covariant factors between T_{2m} anomaly and three areal mean series: ΔZ (S[ΔZ,T_{2m}]) (black solid line), ω_{500} (S[ω_{500},T_{2m}]) (black dashed line) and SR (S[SR,T_{2m}]) (blue solid line)

is significantly correlated with the V_ω and ω_{500}, with correlation coefficients of –0.78 and –0.85, respectively. This indicates that if not taking thermodynamic processes into account, the high-level horizontal wind convergence promotes the downward motion within the air column through the continuity equation of atmosphere, thereby increasing the thickness of the air column.

Therefore, the key local atmospheric dynamic processes that triggered the extreme heat event in August 2022 can be summarized in Fig. 11 and 12. T_{2m} is directly regulated by ΔZ and ω_{500}, since ΔZ and ω_{500} are not independent from each other. The increase in GHT at upper-level atmosphere is a crucial factor in influencing T_{2m}, primarily through modulating ΔZ and ω_{500}. The adjustment of upper-level

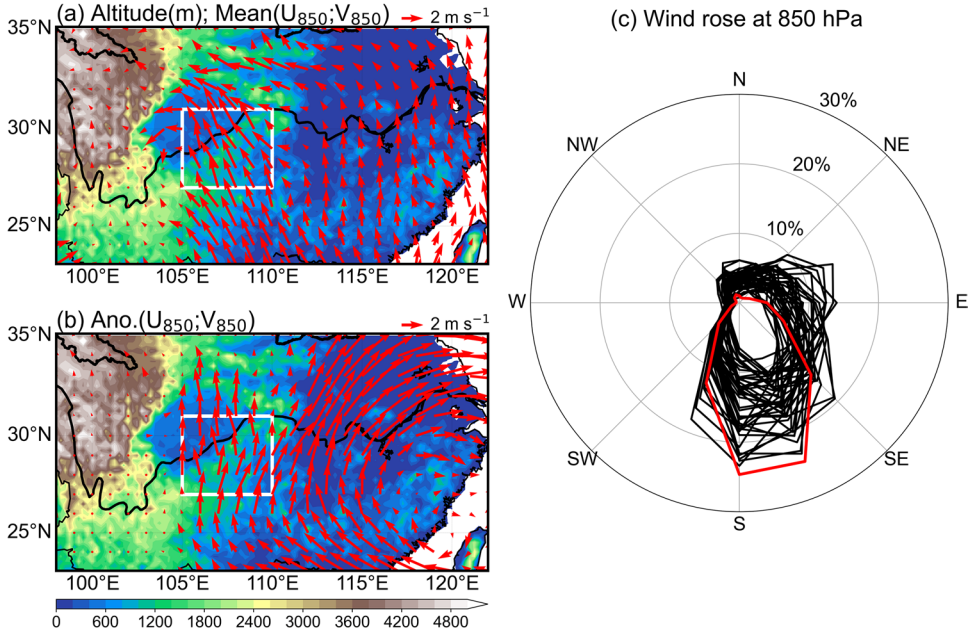

Fig. 15 **a** Altitude (shaded, m) and August climatological horizontal wind (vectors, m s^{-1}) at 850 hPa. **b** Altitude (shaded, m) and anomalous August horizontal wind (vectors, m s^{-1}) at 850 hPa in 2022. The white boxes in **a** and **b** span the Wuling Mountains and are the domains for calculating the frequencies of wind directions (27°-31°N, 105°-110°E). (**c**) Wind rose at 850 hPa within the domain around the southeastern Sichuan Basin, with the red line (black lines) indicating the result in August 2022 (other years from 1979 to 2021)

circulations on ΔZ and ω_{500} is as follows: restricted by the quasi-geostrophic balance, the meridional (zonal) gradient of increased upper-level GHT (around 200 hPa) is closely related to the upper-level zonal (meridional) wind. The meridional gradient of meridional wind leads to upper-level horizontal wind convergence, which favors the enhancement of downward motion between 1000 and 500 hPa. The downward motion contributes to the thickening of the air column. Note that the increase in the upper-level GHT is just one of the important factors influencing ΔZ and ω_{500}, and there are some other factors that can also affect T_{2m} by adjusting ΔZ and ω_{500}.

5 Linkages between local atmospheric dynamic processes and diabatic heating from the land surface

The previous sections focus on the atmospheric dynamic processes associated with extreme heat event over the YRB. Apart from these dynamic processes, the diabatic heating from the underlying surface also exerts a notable influence on T_{2m}. The diabatic processes relevant to T_{2m} include net upward longwave radiation (*LR*), net upward sensible heat flux (*SHF*), and net upward latent heat flux (*LHF*) at the land–atmosphere interface. The regionally averaged time series of these three components are significantly correlated with T_{2m}, with the correlation coefficients of 0.63, 0.71, and 0.72, respectively (Table 3). The correlation coefficient between the sum of these three components and T_{2m} reaches 0.79. *LR*, *SHF*, and *LHF* are primarily influenced by the net downward shortwave radiation (*SR*) received by the underlying surface. The *SR* initially heats the surface, which then heats the overlying atmosphere through upward diabatic heating. *SR* accounts for 99.7% of the variance in the sum of *LR*, *SHF*, and *LHF*. For simplicity, we utilize the regionally averaged *SR* time series to represent the interannual variation of the diabatic heating intensity from the underlying surface.

The multiple correlation coefficient between ΔZ and ω_{500} with T_{2m} is 0.94, which explains 88.1% of the variance in T_{2m} over the YRB. After adding *SR* to the analysis, the multiple correlation coefficient with T_{2m} increases to 0.98, and the explained variance of T_{2m} rises to 95.8% (Table 3). This suggests that atmospheric dynamic processes and diabatic heating processes are not independent but interact with each other. To quantify their relative contributions to T_{2m}, we employ semi-partial correlation analysis. When the *SR*-related component is removed from ω_{500}, ω_{500} becomes uncorrelated with T_{2m}, which indicates that ω_{500} influences T_{2m} mainly through modulating the intensity of incoming *SR*. However, despite the insignificance of correlation between *SR* and T_{2m} after eliminating the ω_{500}-related part from *SR*, *SR* still explains 10.8% of the variance in T_{2m}, which might be attributed to the nonlinear land–atmosphere interactions (Gong et al. 2024; Ni et al. 2024; Zhou 2024).

ΔZ and *SR* increase the T_{2m} through dynamic and thermodynamic processes, respectively (Fig. 13). ω_{500} is closely related to the two processes through thickening the air column to increase ΔZ and reducing the cloud cover to increase *SR*. There is also an interaction between ΔZ and *SR*, which is a positive feedback process. This indicates that there are linkages between the local atmosphere dynamic and thermodynamic processes.The thermodynamic processes are

induced by dynamic processes and react on dynamic processes. When the *SR*-related component is excluded from ΔZ, ΔZ remains significantly correlated with T_{2m}, albeit with a reduced explained variance of 30.2%. After removing the ΔZ-related part from *SR*, *SR* maintains significantly correlated with T_{2m} but explains a decreased variance of 17.1% in T_{2m}, which suggests that atmospheric dynamic processes exhibit a more substantial contribution to T_{2m}. These results demonstrate that both atmospheric dynamic processes and surface diabatic heating processes contribute to T_{2m}, and neither can be substituted for the other.

In August 2022, the areal mean *SR* is transformed into *SHF* and *LR*, which directly heated the surface air, with the *SHF* reaching its historical high (Fig. 14a). The covariant factors of ΔZ, ω_{500}, and *SR* with T_{2m} in 2022 shows that the consistency between ΔZ and T_{2m} was higher than that of ω_{500} or *SR* (Fig. 14b). Thus, the dynamic processes relevant to ΔZ play dominant role in the extreme event in 2022.

6 Conclusions and discussion

In August 2022, the local perturbation thickness of the air column between 1000 and 500 hPa is the key dynamic factor in influencing the surface air temperature, and the sinking motion at 500 hPa plays important roles. By triggering horizontal wind convergence anomalies, the extreme upper-level GHT anomalies intensified the downward motion and thickened the local air column between 1000 and 500 hPa. The exceptionally thickened local air column increased the air temperatures via atmospheric hydrostatic adjustment processes. Meanwhile, increased shortwave radiation led to warmer land surface, which warmed the surface air through diabatic heating processes. There existed a positive feedback between atmospheric dynamic processes and thermodynamic processes which induced this extreme heat event over the YRB, with the former being the dominant contributor.

Apart from the large-scale atmospheric dynamic processes, diabatic heating processes, and nonlinear positive feedback mechanisms, the synoptic-scale foehn effect may also be a crucial local factor influencing the surface temperature in the Sichuan Basin in August 2022. Influenced by the local terrain, the elevation of the Sichuan Basin is lower than its surroundings (Fig. 15a). When southeast winds cross the mountains to the southeast of the Sichuan Basin, particularly the Wuling Mountains (in the white box of Fig. 15), precipitation occurs on the windward slope, and dry air adiabaticly subsidence on the leeward slope, which results in a pronounced warming effect. This study preliminarily analyzes the ERA5 hourly data and finds that, under the influence of local abnormal anticyclones (Fig. 15b), the frequency of southeast winds at 850 hPa over the Wuling Mountains region was significantly higher in 2022 than in other years (Fig. 15c). This may suggest that the frequency of foehn events in the Sichuan Basin was also the highest in 2022. Therefore, large-scale atmospheric dynamic conditions play a fundamental role, the influence of mesoscale and small-scale weather processes on surface temperatures remains a subject and requires further in-depth exploration.

This paper first proposes that the perturbation thickness between 1000 and 500 hPa is a crucial local atmospheric factor influencing the August surface air temperature over the YRB, and it is also the most significant local factor contributing to the extreme heat event in 2022. By referring to the general mechanisms of interannual variation of August surface air temperature, this study analyzes the extreme heat event in August 2022. The present study has the limitation of reliance on linear analysis, which fails to quantify the contributions of nonlinear interactions, such as land–atmosphere interactions. Furthermore, from the perspective of time scale, the natural local variabilities mentioned above are mainly at the interannual scale, yet natural variabilities across other timescales also contribute to this extreme climate event. Specifically, from July 30th to August 29th, a 30–50-day intraseasonal oscillation triggered heatwaves and droughts over the YRB. However, the intensity of this 30–50-day oscillation was slightly above the climatology in August, implying that the seasonal cycle anomalies induced by the underlying conditions may be more crucial for the extremes in August 2022 (Liu et al. 2023).

Besides these local processes, remote air-sea factors played significant roles in indirectly affecting the SAT through influencing the geopotential thickness over the YRB. This extreme event is linked to the negative phase of the Pacific Decadal Oscillation (PDO) and La Niña event (Tang et al. 2023; Yuan et al. 2024). Through the PDO index from the National Oceanic and Atmospheric Administration (NOAA)/Physical Sciences Laboratory and Niño 3.4 index from NOAA/ National Weather Service, we simply calculate the correlation between PDO index, Niño 3.4 index and T_{2m} over the YRB in August (Fig. S1). The result shows that the PDO index and Niño 3.4 index are not highly correlated with T_{2m}, with the correlation coeffients of –0.34 and –0.27, respectively. Meanwhile, both the PDO index and Niño 3.4 index of August are not extremely low in 2022. This indicates that neither PDO or La Niña events dominanted this extreme heat event, and there may exist other remote extreme factors which significantly affected the T_{2m} over the YRB in 2022. We will show the relevant multi-factors in both Northern and Southern Hemisphere in the following work. Consequently, extreme events are often result from a complex interaction across multiple temporal and spatial scales, involving diverse factors and physical processes. To accurately identify these factors

and quantify relevant processes, the development of novel methodologies and theories is imperative.

Supplementary Information The online version contains supplementary material available at https://doi.org/10.1007/s00382-025-07760-2.

Acknowledgements We are thankful to all the data providers.

Author contributions Yue Sun and Jianping Li designed the study and contributed to the data analysis, figures, and writing of the paper. All authors commented on previous versions of the manuscript. All authors read and approved the final manuscript.

Funding This work is supported by the National Natural Science Foundation of China (42288101), Shandong Natural Science Foundation Project (ZR2019ZD12), and Fundamental Research Funds for the Central Universities (202242001).

Data availability The ERA5 monthly reanalysis data on surface (Hersbach et al. 2023a) and pressure level (Hersbach et al. 2023b) can be obtained from https://cds.climate.copernicus.eu/datasets/reanalysis-era5-single-levels-monthly-means?tab=download and https://cds.climate.copernicus.eu/datasets/reanalysis-era5-pressure-levels-monthly-means?tab=download, respectively. The ERA5 hourly reanalysis data on pressure level (Hersbach et al. 2023c) was from https://cds.climate.copernicus.eu/datasets/reanalysis-era5-pressure-levels?tab=download. The surface air temperature observations can be obtained from http://data.cma.cn/en/?r=data/detail&dataCode=A.0012.0001. The PDO index is from https://psl.noaa.gov/data/timeseries/month/PDO/ and the Niño 3.4 index is from https://origin.cpc.ncep.noaa.gov/products/analysis_monitoring/ensostuff/ONI_v5.php.

Declarations

Conflict of interests The authors have no relevant financial or non-financial interests to disclose.

References

Bannon PR (1995) Hydrostatic adjustment: Lamb's problem. J Atmos Sci 52:1743–1752. https://doi.org/10.1175/1520-0469(1995)052%3c1743:HALP%3e2.0.CO;2

Bannon PR (1996) Nonlinear hydrostatic adjustment. J Atmos Sci 53:3606–3617. https://doi.org/10.1175/1520-0469(1996)053%3c3606:NHA%3e2.0.CO;2

Bretherton CS, Widmann M, Dymnikov VP, Wallace JM, Bladé I (1999) The effective number of spatial degrees of freedom of a time-varying field. J Clim 12:1990–2009. https://doi.org/10.1175/1520-0442(1999)012%3c1990:TENOSD%3e2.0.CO;2

Chagnon JM, Bannon PR (2001) Hydrostatic and geostrophic adjustment in a compressible atmosphere: Initial response and final equilibrium to an instantaneous localized heating. J Atmos Sci 58:3776–3792. https://doi.org/10.1175/1520-0469(2001)058%3c3776:HAGAIA%3e2.0.CO;2

Cui X, Liu Y, Ai X, Wang L, Wang M (2015) Mechanism study on vertical hydrostatic adjustment procedure. J Meteorol Sci 35:462–467 ((**in Chinese with English abstract**))

Cui XD, Liu YD, Zhao ZL (2016) Study of characteristics of the acoustic gravity wave and energy conversion in the three-dimensional hydrostatic adjustment process. Acta Meteorol Sinica 74:127–132 ((**in Chinese with English abstract**))

Darand M (2020) Spatiotemporal analysis of the relationship between near-surface air temperature and troposphere thickness over Iran. Meteorol Appl 27:e1907. https://doi.org/10.1002/met.1907

Dubey AK, Kumar P (2023) Future projections of heatwave characteristics and dynamics over India using a high-resolution regional earth system model. Clim Dyn 60:127–145. https://doi.org/10.1007/s00382-022-06309-x

Fischer EM, Seneviratne SI, Vidale PL, Lüthi D, Schär C (2007) Soil moisture–atmosphere interactions during the 2003 European summer heat wave. J Clim 20:5081–5099. https://doi.org/10.1175/JCLI4288.1

Gong H, Ma K, Hu Z, Dong Z, Ma Y, Chen W, Wu R, Wang L (2024) Attribution of the August 2022 extreme heatwave in Southern China: role of dynamical and thermodynamical processes. Bull Am Meteor Soc 105:E193–E199. https://doi.org/10.1175/BAMS-D-23-0175.1

Hayashi Y (1982) Confidence intervals of a climatic signal. J Atmos Sci 39:1895–1905

He C, Zhou T, Zhang L, Chen X, Zhang W (2023) Extremely hot East Asia and flooding western South Asia in the summer of 2022 tied to reversed flow over Tibetan Plateau. Clim Dyn 61:2103–2119. https://doi.org/10.1007/s00382-023-06669-y

Hersbach H, Bell B, Berrisford P et al (2020) The ERA5 global reanalysis. Quarterly J Royal Meteorol Soc 146:1999–2049. https://doi.org/10.1002/qj.3803

Hersbach H, Bell B, Berrisford P, Biavati G, Horányi A, Muñoz Sabater J, Nicolas J, Peubey C, Radu R, Rozum I, Schepers D, Simmons A, Soci C, Dee D, Thépaut J-N (2023a) ERA5 monthly averaged data on single levels from 1940 to present. Copernicus Climate Change Service (C3S) Climate Data Store (CDS). https://doi.org/10.24381/cds.f17050d7. (Accessed on 05-Mar.-2025)

Hersbach H, Bell B, Berrisford P, Biavati G, Horányi A, Muñoz Sabater J, Nicolas J, Peubey C, Radu R, Rozum I, Schepers D, Simmons A, Soci C, Dee D, Thépaut J-N (2023b) ERA5 monthly averaged data on pressure levels from 1940 to present. Copernicus Climate Change Service (C3S) Climate Data Store (CDS). https://doi.org/10.24381/cds.6860a573. (Accessed on 05-Mar.-2025)

Hersbach H, Bell B, Berrisford P, Biavati G, Horányi A, Muñoz Sabater J, Nicolas J, Peubey C, Radu R, Rozum I, Schepers D, Simmons A, Soci C, Dee D, Thépaut J-N (2023c) ERA5 hourly data on pressure levels from 1940 to present. Copernicus Climate Change Service (C3S) Climate Data Store (CDS). https://doi.org/10.24381/cds.bd0915c6. (Accessed on 05-Mar.-2025)

Holton JR, Hakim GJ (2013) *An introduction to dynamic meteorology* (Vol. 88). Academic press, 552 pp. https://doi.org/10.1016/C2009-0-63394-8.

Hoskins BJ, Karoly DJ (1981) The steady linear response of a spherical atmosphere to thermal and orographic forcing. J Atmos Sci 38:1179–1196. https://doi.org/10.1175/1520-0469(1981)038%3c1179:TSLROA%3e2.0.CO;2

Hu Z, Zou G (1991) Atmospheric non-static equilibrium model and elastic adaptation. Sci China B 21:550–560. https://doi.org/10.1360/zb1991-21-5-550

Hua W, Dai A, Qin M, Hu Y, Cui Y (2023) How unexpected was the 2022 summertime heat extremes in the middle reaches of the Yangtze River? Geophys Res Lett 50:e2023GL104269. https://doi.org/10.1029/2023GL104269

Huang Z, Tan X, Liu B (2024) Relative contributions of large-scale atmospheric circulation dynamics and anthropogenic warming to the unprecedented 2022 Yangtze River Basin heatwave. J Geophys Res: Atmos 129:e2023JD039330. https://doi.org/10.1029/2023JD039330

Huang J (1990) Meteorological statistical analysis and forecasting methods. *Meteorological Press*. 15pp. (in Chinese)

Jiang J, Liu Y, Mao J, Wu G (2023) Extreme heatwave over Eastern China in summer 2022: the role of three oceans and local soil

moisture feedback. Environ Res Lett 18:044025. https://doi.org/10.1088/1748-9326/acc5fb/meta
Kim S (2015) ppcor: an R package for a fast calculation to semi-partial correlation coefficients. Commun Statis Appl Meth 22:665. https://doi.org/10.5351/CSAM.2015.22.6.665
Li J, Sun C, Jin FF (2013) NAO implicated as a predictor of Northern Hemisphere mean temperature multidecadal variability. Geophys Res Lett 40:5497–5502. https://doi.org/10.1002/2013GL057877
Li Y, Li J, Jin FF, Zhao S (2015) Interhemispheric propagation of stationary Rossby waves in a horizontally nonuniform background flow. J Atmos Sci 72:3233–3256. https://doi.org/10.1175/JAS-D-14-0239.1
Li J, Xie T, Tang X, Wang H, Sun C, Feng J, Zheng F, Ding R (2022) Influence of the NAO on wintertime surface air temperature over East Asia: Multidecadal variability and decadal prediction. Adv Atmos Sci 39:625–642. https://doi.org/10.1007/s00376-021-1075-1
Liao Z, Yuan YF, Chen Y, Zhai PM (2024) Extraordinary hot extreme in summer 2022 over the Yangtze River basin modulated by the La Niña condition under global warming. Adv Clim Chang Res 15:21–30. https://doi.org/10.1016/j.accre.2023.12.006
Liu B, Zhu C, Ma S, Yan Y, Jiang N (2023) Subseasonal processes of triple extreme heatwaves over the Yangtze River Valley in 2022. Weather Clim Extreme 40:100572. https://doi.org/10.1016/j.wace.2023.100572
Lu R, Xu K, Chen R, Chen W, Li F, Lv C (2023) Heat waves in summer 2022 and increasing concern regarding heat waves in general. Atmos Ocean Sci Lett 16:100290. https://doi.org/10.1016/j.aosl.2022.100290
Massie DR, Rose MA (1997) Predicting daily maximum temperatures using linear regression and Eta geopotential thickness forecasts. Weather Forecast 12:799–807. https://doi.org/10.1175/1520-0434(1997)012%3c0799:PDMTUL%3e2.0.CO;2
Miralles DG, Gentine P, Seneviratne SI, Teuling AJ (2019) Land–atmospheric feedbacks during droughts and heatwaves: state of the science and current challenges. Ann N Y Acad Sci 1436:19–35. https://doi.org/10.1111/nyas.13912
Ni Y, Qiu B, Miao X, Li L, Chen J, Tian X, Zhao S, Guo W (2024) Shift of soil moisture-temperature coupling exacerbated 2022 compound hot-dry event in eastern China. Environ Res Lett 19:014059
Pan S, Yin Z, Duan M, Han T, Fan Y, Huang Y, Wang H (2024) Seasonal prediction of extreme high-temperature days over the Yangtze River basin. Sci China Earth Sci 67:1–11. https://doi.org/10.1007/s11430-023-1265-2
Plumb RA (1985) On the three-dimensional propagation of stationary waves. J Atmos Sci 42:217–229. https://doi.org/10.1175/1520-0469(1985)042%3c0217:OTTDPO%3e2.0.CO;2
Qiao L, Zuo Z, Zhang R, Piao S, Xiao D, Zhang K (2023) Soil moisture–atmosphere coupling accelerates global warming. Nat Commun 14:4908. https://doi.org/10.1038/s41467-023-40641-y
Rose M (2000) Using 1000–925 MB Thickness in Forecasting Minimum Temperature. Nashville, TN, Technical Attachment SR/SSD 2000–25. Silver Spring, MD: National Weather Service, National Oceanic and Atmospheric Administration (NOAA). https://www.weather.gov/ohx/mintemps. (Accessed on 05-Mar.-2025)
Rousta I, Doostkamian M, Olafsson H, Ghafarian-Malamiri HR, Zhang H, Taherian AM, Sarif MO, Gupta RD, Monroy-Vargas ER (2019) On the relationship between the 500 hPa height fluctuations and the atmosphere thickness over Iran and the Middle East. Tethys 16:3–14
Shaman J, Samelson RM, Tziperman E (2012) Complex wavenumber Rossby wave ray tracing. J Atmos Sci 69:2112–2133. https://doi.org/10.1175/JAS-D-11-0193.1
Sotack T, Bannon PR (1999) Lamb's hydrostatic adjustment for heating of finite duration. J Atmos Sci 56:71–81. https://doi.org/10.1175/1520-0469(1999)056%3c0071:LSHAFH%3e2.0.CO;2
Struthwolf ME (1995) Forecasting maximum temperatures through use of an adjusted 850-to 700-mb thickness technique. Weather Forecast 10:160–171. https://doi.org/10.1175/1520-0434(1995)010%3c0160:FMTTUO%3e2.0.CO;2
Sun Y, Li J, Wang H, Li R, Tang X (2023) Extreme rainfall in Northern China in September 2021 tied to air–sea multi-factors. Clim Dyn 60:1987–2001. https://doi.org/10.1007/s00382-022-06439-2
Takaya K, Nakamura H (2001) A formulation of a phase-independent wave-activity flux for stationary and migratory quasigeostrophic eddies on a zonally varying basic flow. J Atmos Sci 58:608–627
Tang S, Qiao S, Wang B, Liu F, Feng T, Yang J, He M, Chen D, Cheng J, Feng G, Dong W (2023) Linkages of unprecedented 2022 Yangtze River Valley heatwaves to Pakistan flood and triple-dip La Niña. Npj Clim Atmos Sci 6:44. https://doi.org/10.1038/s41612-023-00386-3
Thompson DW, Wallace JM (1998) The Arctic Oscillation signature in the wintertime geopotential height and temperature fields. Geophys Res Lett 25:1297–1300. https://doi.org/10.1029/98GL00950
Thompson V, Kennedy-Asser AT, Vosper E, Lo YE, Huntingford C, Andrews O, Collins M, Hegerl GC, Mitchell D (2022) The 2021 western North America heat wave among the most extreme events ever recorded globally. Sci Adv 8:eabm6860. https://doi.org/10.1126/sciadv.abm6860
Trenberth KE (1984) Interannual variability of the Southern Hemisphere circulation: Representativeness of the year of the global weather experiment. Mon Weather Rev 112:108–123. https://doi.org/10.1175/1520-0493(1984)112%3c0108:IVOTSH%3e2.0.CO;2
Wallace JM, Zhang Y, Lau KH (1993) Structure and seasonality of interannual and interdecadal variability of the geopotential height and temperature fields in the Northern Hemisphere troposphere. J Clim 6:2063–2082. https://doi.org/10.1175/1520-0442(1993)006%3c2063:SASOIA%3e2.0.CO;2
Wang P, Zhang Q, Yang Y, Tang J (2019) The sensitivity to initial soil moisture for three severe cases of heat waves over Eastern China. Front Environ Sci 7:18. https://doi.org/10.3389/fenvs.2019.00018
Wang Z, Luo H, Yang S (2023) Different mechanisms for the extremely hot central-eastern China in July-August 2022 from a Eurasian large-scale circulation perspective. Environ Res Lett 18:024023. https://doi.org/10.1088/1748-9326/acb3e5
Wei W, Zhang R, Wen M, Kim BJ, Nam JC (2015) Interannual variation of the South Asian high and its relation with Indian and East Asian summer monsoon rainfall. J Clim 28:2623–2634. https://doi.org/10.1175/JCLI-D-14-00454.1
Whitham GB (1960) A note on group velocity. J Fluid Mech 9:347–352. https://doi.org/10.1017/S0022112060001158
Xia J, Chen J, She D (2022) Impacts and countermeasures of extreme drought in the Yangtze River Basin in 2022. J Hydra Eng 53:1143–1153 (**(in Chinese with English abstract)**)
Yasui S, Watanabe M (2010) Forcing processes of the summertime circumglobal teleconnection pattern in a dry AGCM. J Clim 23:2093–2114. https://doi.org/10.1175/2009jcli3323.1
Ye D, Li M (1965) Adaptation problems in atmospheric motion. Science Press. 4 pp. (in Chinese)
Yin Z, Yang S, Wei W (2023) Prevalent atmospheric and oceanic signals of the unprecedented heatwaves over the Yangtze River Valley in July–August 2022. Atmos Res 295:107018. https://doi.org/10.1016/j.atmosres.2023.107018
You Y, Furtado JC (2017) The role of South Pacific atmospheric variability in the development of different types of ENSO. Geophys Res Lett 44:7438–7446. https://doi.org/10.1002/2017GL073475

Yuan Y, Liao Z, Zhou B, Zhai P (2023) Unprecedented Hot Extremes Observed in City Clusters in China during Summer 2022. J Meteorol Res 37:141–148. https://doi.org/10.1007/s13351-023-2184-9

Yuan X, Wang Y, Zhou S, Li H, Li C (2024) Multiscale causes of the 2022 Yangtze mega-flash drought under climate change. Sci China Earth Sci 67:2649–2660. https://doi.org/10.1007/s11430-024-1356-x

Zar JH, 1984: Biostatistical Analysis. Prentice Hall, 718 pp.

Zeng Q (1963) The influence of disturbance characteristics on atmospheric adaptation process and the use of wind measurement data. Acta Meteor Sin 33:37–50 (**(in Chinese)**)

Zhang J, Wu L (2011) Land-atmosphere coupling amplifies hot extremes over China. Chinese Sci Bull 56:3328–3332. https://doi.org/10.1007/s11434-011-4628-3

Zhang T, Deng Y, Chen J, Yang S, Dai Y (2023a) An energetics tale of the 2022 mega-heatwave over central-eastern China. Npj Clim Atmos Sci 6:162. https://doi.org/10.1038/s41612-023-00490-4

Zhang D, Chen L, Yuan Y, Zuo J, Ke Z (2023b) Why was the heat wave in the Yangtze River valley abnormally intensified in late summer 2022? Environ Res Lett 18:034014. https://doi.org/10.1088/1748-9326/acba30

Zhao S, Li J, Li Y (2015) Dynamics of an interhemispheric teleconnection across the critical latitude through a southerly duct during boreal winter. J Clim 28:7437–7456. https://doi.org/10.1175/JCLI-D-14-00425.1

Zhao S, Li J, Li Y, Jin FF, Zheng J (2019) Interhemispheric influence of Indo-Pacific convection oscillation on Southern Hemisphere rainfall through southward propagation of Rossby waves. Clim Dyn 52:3203–3221. https://doi.org/10.1007/s00382-018-4324-y

Zhong W, Cai W, Sullivan A, Duan W, Yang S (2023) Seasonally alternate roles of the North Pacific Oscillation and the South Pacific Oscillation in tropical Pacific zonal wind and ENSO. J Clim 36:4393–4411. https://doi.org/10.1175/JCLI-D-22-0461.1

Zhou T (2024) The dry-hot feedback between soil moisture and atmosphere and the accelerated global warming. Sci China Earth Sci 67:890–891. https://doi.org/10.1007/s11430-023-1281-y